On the Very Bright Dropouts Selected Using the James Webb Space Telescope NIRCam Instrument

Bangzheng Sun and Haojing Yan
Department of Physics and Astronomy, University of Missouri, 701 South College Avenue, Columbia, MO 65201, USA
Received 2025 February 8; revised 2025 April 27; accepted 2025 May 20; published 2025 June 27

Abstract

The selection of candidate high-redshift galaxies using the dropout technique targeting the Lyman-break signature sometimes yields very bright objects that are too luminous to be easily explained if they are indeed at the expected redshifts. Here, we present systematic study of very bright dropouts selected through successive bands of the NIRCam instrument onboard the James Webb Space Telescope (JWST). Using the public NIRCam data in four blank fields over 500 arcmin^2, 300 such objects were found. They have F356W magnitudes <25.1 mag or <26.0 mag depending on the dropout passband, and the majority of them ($>80\%$) have very red F115W $-$ F356W colors >2.0 mag, qualifying them as "extremely red objects." We focus on 137 objects that also have mid-infrared observations from the JWST MIRI instrument. Their spectral energy distribution analysis shows that these objects are dominated by low-redshift ($z \sim 1$–4) galaxies ($\gtrsim 67\%$). However, a non-negligible fraction ($\gtrsim 7\%$) could be at high redshifts. Seven of our objects have secure spectroscopic redshifts from JWST NIRSpec identifications, and the results confirm this picture: while six are low-redshift galaxies ($z \approx 3$), one is a known galaxy at $z = 8.679$ (with $M_{\rm UV} = -22.4$ mag and stellar mass $M_* = 10^{9.1} M_\odot$) recovered in our sample. In light of recent theoretical models on early galaxy formation, this confirmed high-redshift galaxy does not pose a challenge. However, since our sample contains very luminous high-redshift candidates in the regime still underexplored ($M_{\rm UV} \leqslant -23$ mag and $M_* > 10^{10.5} M_\odot$), spectroscopic identifications are necessary to ensure they do not create tension with these new models.

Unified Astronomy Thesaurus concepts: High-redshift galaxies (734); Starburst galaxies (1570)

1. Introduction

Various kinds of "extremely red objects" (EROs) have been selected over the past three decades by using different color indices involving different infrared (IR) bands as the technologies evolve. The early discoveries were mostly made by comparing the ground-based observations in K band ($\sim 2.2\,\mu$m) and in an optical band (e.g., R. Elston et al. 1988; E. M. Hu & S. E. Ridgway 1994; D. Thompson et al. 1999; M. Scodeggio & D. R. Silva 2000), although occasionally deep data in the less red F160W band ($\sim 1.6\,\mu$m) of the Hubble Space Telescope (HST) Near Infrared Camera and Multi-Object Spectrometer were also used (e.g., L. Yan et al. 2000). The general interpretation of such EROs is that they are predominantly early-type galaxies at $z \approx 1$ and that their red IR-to-optical colors are due to their old stellar populations. After the launch of the Spitzer Space Telescope, the ERO selection proceeded to using the Infrared Array Camera (IRAC) 3.6 and/or 4.5 μm channels in IR and the HST Advanced Camera for Surveys (ACS) bands in optical (e.g., H. Yan et al. 2004). Such EROs are also mostly evolved galaxies but are at higher redshifts of $z \approx 2$–4. The extension in the IR wavelengths by IRAC also allowed the ERO selection through IR colors such as $K_s - 4.5\,\mu$m involving ground-based K_s band (e.g., W.-H. Wang et al. 2012) and F160W $-$ 4.5 μm involving the reddest band (F160W) of the HST Wide Field Camera 3 (WFC3) (e.g., K. I. Caputi et al. 2014; T. Wang et al. 2016; B. Alcalde Pampliega et al. 2019). The latter ones are also referred to as the "HST-dark" objects because they are extremely weak or even invisible in the deep images taken in

any HST bands. Interestingly, the EROs selected using IR color indices consist of not only early-type galaxies dominated by passively evolving stellar populations but also extremely dust-reddened galaxies with strong ongoing star formation embedded by dust (e.g., T. Wang et al. 2019). In fact, dusty starbursts invisible at $\lambda < 2\,\mu$m were already known to exist, for instance, the historical submillimeter galaxy (SMG) HDF 850.1 (L. L. Cowie et al. 2009; F. Walter et al. 2012). Many similar SMGs were later revealed (e.g., L. Zhou et al. 2020; C. Gómez-Guijarro et al. 2022; M. Y. Xiao et al. 2023), making them a distinct population among EROs at $z > 4$ awaiting further exploration.

In a broad sense, the selection of high-redshift (high-z) galaxies also relies on identifying red colors, which are due to the Lyman-break signature in their spectral energy distributions (SEDs). This is caused by the discrete neutral hydrogen clouds along the sightline that absorb photons bluer than the Lyman-limit (rest frame $\lambda < 912\,\text{Å}$) and those coinciding with the Lyα line wavelength (rest frame $\lambda = 1216\,\text{Å}$). These absorptions create a sharp discontinuity ("Lyman break") in the spectrum of a high-redshift (high-z) galaxy, resulting in a red color index in two adjacent bands that straddle the Lyman break. For this reason, a high-z galaxy would appear to "dropout" from the band to the blue side of the break and be visible in bands redder than the break, and this is the basis of the classic "dropout" selection of galaxies at $z \gtrsim 3$ (C. C. Steidel & D. Hamilton 1992, 1993; C. C. Steidel et al. 1995). At $z > 5$, the cumulative Lyα line absorptions ("Lyα forest") are so strong that the Lyman break occurs at the rest frame 1216 Å. In practice, candidate high-z galaxies selected based on the Lyman-break signature always have contaminants from red galaxies at low redshifts ("low-z interlopers"), and the most extreme ones could be the aforementioned EROs (see, e.g., P. Arrabal Haro et al. 2023a; J. A. Zavala et al. 2023).

Table 1
Summary of the Fields Used in this Work, which have Data from both NIRCam and MIRI

Field	R.A. (deg)	Decl. (deg)	Instrument	Pipeline	Context	Area (arcmin^2)	MIRI Overlap (arcmin^2)	Exposure (ks)
COSMOS	150.12299	2.34764	NIRCam	1.10.2	1089	137.13	67.80	∼2.5
	…	…	MIRI	1.12.5	1183	100.58	…	∼1.7
UDS	34.35004	−5.20001	NIRCam	1.10.2/1.11.3	1089/1106	185.83	76.91	∼1–4
	…	…	MIRI	1.12.5	1180	112.51	…	∼1.7
CEERS	215.00545	52.93451	NIRCam	1.9.4	1046	86.45	3.72−7.69	∼2.5
	…	…	MIRI	1.12.5	1183	∼5−16	…	∼1–8
JADES (deep)	53.16444	−27.78256	NIRCam	1.12.5	1180	25.50	20.83	∼14–60
JADES (medium)	53.07011	−27.90011	NIRCam	1.12.4	1140	37.94	15.99	∼1.5–40
GOODS-S	53.14027	−27.82140	MIRI	1.13.4	1188	32.90	…	∼0.6–142

Note. The nominal exposure times in these fields are given under "Exposure." The equatorial coordinates are at the field centers, and the sizes of the overlapped regions between the NIRCam and the MIRI coverages are indicated in the "MIRI Overlap" column. The version of the JWST data reduction pipeline that we used and the relevant context file ("pmap") are listed under "Pipeline" and "Context," respectively. The astrometry that we adopted in the COSMOS, UDS, and CEERS fields is that from the HST CANDELS survey, while that in the JADES fields are based on the GAIA DR3.

The James Webb Space Telescope (JWST) offers unprecedented sensitivity and spatial resolution in the IR wavelengths. It has pushed the redshift record of galaxies to $z = 14.32$ (S. Carniani et al. 2024), and thousands of candidates have been selected at $z \gtrsim 7$ using its NIRCam instrument. In the meantime, it has also brought the study of EROs to a new level (e.g., L. Barrufet et al. 2023; C. Gómez-Guijarro et al. 2023; E. J. Nelson et al. 2023; G. Rodighiero et al. 2023; J. L. Gibson et al. 2024). When the hunt for high-z galaxies moves forward to higher and higher redshifts, the selected candidates bear more and more similarity to EROs. As an example, galaxies at $z \gtrsim 12$ should be invisible at $\lambda < 1.5 \mu$m, which could be regarded as being HST-dark.

On face value, all known EROs are IR-bright. For instance, typical HST-dark galaxies have AB magnitudes of $\leqslant 24$ mag at 3–5 μm. Therefore, one might think that the IR brightness could be used to distinguish the two populations. However, EROs being IR-bright reflect more the limitation of the technology at the time when they were first studied than their intrinsic properties. In this context, it is important to study how these two populations overlap in the new JWST era, starting from the bright end. In this work, we aim at the very bright high-z candidates selected using the NIRCam data following the classic dropout technique and investigate how they could be affected by low-z EROs. In order to make our analysis robust, we focus on the fields where the mid-IR imaging data from the JWST MIRI instrument are also available.

The structure of our paper is as follows. We describe the relevant NIRCam and MIRI data in Section 2 and the photometry in Section 3, respectively. The selection of bright dropouts in the NIRCam bands is detailed in Section 4, followed by the analysis of their SEDs in Section 5. Based on their photometric redshifts ($z_{\rm phot}$), these bright dropouts are broadly categorized as being potential high-z galaxies and possible low-z EROs. A small fraction of our objects have spectroscopic confirmations, which we show in Section 6. We discuss our results in Section 7. and conclude with a summary in Section 8. All magnitudes quoted in this work are in the AB system (J. B. Oke & J. E. Gunn 1983). All coordinates are in the ICRS frame and Equinox 2000. We adopt a flat ΛCDM cosmology with $H_0 = 71$ km s^{-1} Mpc^{-1}, $\Omega_m = 0.27$, and $\Omega_\Lambda = 0.73$.

2. JWST NIRCam and MIRI Imaging Data

We utilize four JWST fields that have both NIRCam and MIRI data, which are summarized in Table 1. These are from the Public Release Imaging for Extragalactic Research (PRIMER) program (PI J. Dunlop) in the COSMOS and the UDS fields, the Cosmic Evolution Early Release Science Survey (CEERS; S. L. Finkelstein et al. 2025) in the EGS field, and the JWST Advanced Deep Extragalactic Survey (JADES; D. J. Eisenstein et al. 2023) in the GOODS-S region. Table 2 shows the averaged 2σ depths in each NIRCam and MIRI passband and in each field. These data and their reductions are briefly described below.

2.1. Data Description

1. *PRIMER in COSMOS and UDS*. Two shallow but wide fields. The total areas covered by NIRCam are 137.13 and 185.83 arcmin^2, respectively, and those covered by MIRI are 100.58 and 112.51 arcmin^2, respectively. The PRIMER program executed the MIRI observations as the primary and the NIRCam ones as the coordinated parallel while maximizing the overlapping areas between the two. In the end, the overlapping areas between the NIRCam and MIRI observations are 67.80 and 76.91 arcmin^2 for these two fields, respectively. The NIRCam observations utilized eight passbands: F090W, F115W, F150W, and F200W in the short-wavelength channel (SW), and F277W, F356W, F410M, and F444W in the long-wavelength (LW) channel. The MIRI observations were in F770W and F1800W. In these two fields, we selected dropouts in F090W, F115W, F150W, F200W, and F277W. To assist the F090W dropout selection, we integrated the HST ACS data from the CANDELS survey (N. A. Grogin et al. 2011; A. M. Koekemoer et al. 2011) in both COSMOS and UDS.

2. *CEERS in EGS*. Another shallow but wide field. It was observed in seven NIRCam bands: F115W, F150W, and F200W in the SW channel, and F277W, F356W, F410M, and F444W in the LW channel. The NIRCam coverage is 86.45 arcmin^2. The MIRI observations were made in smaller areas and were in seven bands: F560W, F770W,

Table 2
Averaged 2σ Depth in Each Passband for the Fields in Table 1, Measured in a $r = 0\rlap{.}''2$ Circular Aperture on the rms Maps

Field (NIRCam)	F090W	F115W	F150W	F200W	F277W	F335M	F356W	F410M	F444W
CEERS	⋯	28.5	28.5	29.4	29.5	⋯	29.0	28.8	29.3
UDS	28.1	28.1	28.3	28.4	29.0	⋯	29.2	28.4	28.9
COSMOS	28.2	28.2	28.4	28.6	29.2	⋯	29.3	28.6	29.0
JADES (deep)	30.4	30.7	30.6	30.6	31.0	30.4	30.8	30.5	30.8
JADES (medium)	29.2	28.5	29.0	28.8	29.2	30.0	29.8	29.6	29.0

Field (MIRI)	F560W	F770W	F1000W	F1280W	F1500W	F1800W	F2100W	F2550W
CEERS	26.8	26.0	26.5	26.1	25.8	25.0	25.4	⋯
UDS	⋯	27.3	⋯	⋯	⋯	25.3	⋯	⋯
COSMOS	⋯	27.3	⋯	⋯	⋯	25.3	⋯	⋯
GOODS-S	27.1	27.5	26.3	26.1	26.1	25.0	25.1	23.2

Note. The limits adopted for a specific object in case of nondetection are based on the local depths at the source position, which could be different from these averaged depths.

F1000W, F1280W, F1500W, F1800W, and F2100W. However, the MIRI footprints are nonoverlapping for all these bands, and different parts of the field are covered only by certain sets of filters: (1) F560W and F770W (7.69 arcmin^2 overlapping with NIRCam), (2) F1000W, F1280W, F1500W, and F1800W (3.72 arcmin^2 overlapping with NIRCam), (3) F1500W only (5.15 arcmin^2 overlapping with NIRCam), and (4) F2100W only (no overlap with NIRCam). Due to the lack of the F090W data, we only searched for the F115W, F150W, F200W, and F277W dropouts. We utilized the ancillary HST ACS data from the CANDELS survey to assist the F115W dropout selection.

3. *GOODS-S*. The main part of the data is from JADES (D. J. Eisenstein et al. 2023), which made the NIRCam observations in two areas within the GOODS-S field at two different depths, "deep" and "medium" (hereafter JADES-deep and JADES-medium). The data were taken in nine NIRCam bands: F090W, F115W, F150W, and F200W in the SW channel, and F277W, F335M, F356W, F410M, and F444W in the LW channel. These data are all much deeper than PRIMER and CEERS. We also integrated the NIRCam data from the Pure Parallel Wide Area Legacy Imaging Survey (PANORAMIC, PID 2514; C. C. Williams et al. 2025) and those from PID 3215 (PI D. Eisenstein) into the JADES-medium field. The final NIRCam images cover 25.50 and 37.94 arcmin^2 in JADES-deep and JADES-medium, respectively. For MIRI, we combined all the public observations overlapping the JADES coverage into one mosaic per band, which include those from PID 1207 (PI G. Rieke), 1283 (PI H. Norgaard-Nielsen), and 1180 (PI D. Eisenstein). Eight MIRI bands were utilized by these programs: F560W, F770W, F1000W, F1280W, F1500W, F1800W, F2100W, and F2550W, and the final MIRI images cover 32.90 arcmin^2 in all eight bands. The overlapping areas between NIRCam and MIRI are 20.83 and 15.99 arcmin^2 in JADES-deep and JADES-medium, respectively. Unfortunately, another JADES field, GOODS-N, did not have overlapped NIRCam and MIRI imaging data at the time of this study; therefore, it was not included in this work.

2.2. Data Reduction

We reduced all the data in this study on our own using the JWST pipeline (H. Bushouse et al. 2024). The NIRCam data reduction followed the procedures outlined in H. Yan et al. (2023b) and H. Yan et al. (2024). For MIRI, we ran through the similar procedures but with four changes: (1) in the `calwebb_detector1` step, we set `jump.find_showers` to "True" to remove the large residuals on single MIRI exposures due to strong cosmic ray events; (2) for the products after the stage 2 pipeline process, we followed the recipe by G. Yang et al. (2023) to remove the stripe-like noise pattern in horizontal and/or vertical directions; (3) following the same recipe, we then constructed a background image on a per-observation and per-filter basis by first masking the source and then taking the median of all single exposures, which was used as the template to remove the remaining noise patterns; and (4) we excluded the coronagraph areas in each individual exposure by masking their pixels to `DO_NOT_USE` in the data quality array.

3. Photometry

All the final NIRCam and MIRI mosaics have a pixel scale of $0\rlap{.}''06$, which translates to the AB magnitude zero-point of 26.581. We used `SExtractor` (E. Bertin & S. Arnouts 1996) for source extraction and photometry. We treated the NIRCam and the MIRI images separately because the latter have much larger point spread functions (PSFs).

3.1. NIRCam Photometry for Dropout Selection

The dropout selection involves the NIRCam data but not the MIRI data. For each field, we ran `SExtractor` in the dual-image mode and adopted F356W-based match-aperture photometry. We chose the F356W band as the detection band for the following reasons: (1) the F356W images are usually the deepest across all bands; (2) the PSF in this band is sufficiently large, which ensures that the apertures properly determined in this band include all source fluxes in any bluer bands; and (3) the F356W images present a notably cleaner background than those in the SW bands.

The source extraction was done by applying a 5×5 Gaussian convolution filter with a full width at half-maximum (FWHM) of 2 pixels. From the weight images produced by the

JWST data reduction pipeline, we derived the "rms" maps using the `astroRMS` routine,[1] which calculates the auto-correlation of the science image pixels due to the drizzling process that should be applied to scale the weight images. These rms maps were used for both the source detection and the estimate of photometric errors. The detection and analysis thresholds were set to 1.0 in SExtractor. We adopted the `MAG_ISO` magnitudes and only retained the sources with signal-to-noise ratio (S/N) of at least 5 and ISOAREA of at least 10 pixels in the F356W image.

3.2. Photometry for Spectral Energy Distributions

When constructing SEDs, a common practice is to use photometry on PSF-matched images, i.e., the images in different bands are all convolved to have the same PSF size as in the band that has the largest PSF. Our SED analysis would involve both the NIRCam and the MIRI data, and PSF-matched photometry across all bands would not be appropriate in this case: smearing the NIRCam data (PSF FWHM $0\rlap{.}''030$ to $0\rlap{.}''145$ from F090W to F444W) to the coarsest MIRI resolution (F2550W PSF FWHM of $\sim 0\rlap{.}''803$) would blend many unrelated neighbors in the NIRCam images and corrupt the NIRCam photometry.

As the best compromise, we took a hybrid approach. In the NIRCam wavelengths, we prepared another set of NIRCam photometry done on the PSF-matched NIRCam images. For each field, we convolved the images in the bluer bands to the PSF size of the F444W image. The PSFs were derived using isolated stars in the field, following the procedure in C. Ling & H. Yan (2022). SExtractor was again run in the dual-image mode, and this time the F444W image was used as the basis. We again adopted the `MAG_ISO` magnitudes to calculate the colors. A common practice would be to scale up the `MAG_ISO`-based SED to the "total flux" SED by adding the difference between the `MAG_ISO` and the `MAG_AUTO` magnitude in F444W band. However, a considerable fraction of our objects have close neighbors that would contaminate the `MAG_AUTO` measurements, e.g., f115d_brt_cosmos_344 and f150d_brt_cosmos_093 shown in Figure 1. Therefore, we chose not to apply such a correction. For isolated, bright ($m_{444} < 26.5$ mag) sources, we found that the differences between the `MAG_ISO` and the `MAG_AUTO` magnitudes were under 0.05 mag, and the impact of omitting such a correction would only be marginal to the SED analysis.

The MIRI PSF size varies greatly in different bands, which makes the PSF-matched photometry also inappropriate among the MIRI images. Therefore, we ran SExtractor in the single-image mode for each MIRI band and adopted the `MAG_ISO` magnitudes. Similar to what was mentioned above for the NIRCam images, we also found that the difference between the `MAG_ISO` and the `MAG_AUTO` magnitudes were under 0.05 mag for bright, isolated sources in the MIRI images.

Finally, we note that we treated any photometry with S/N < 2 as nondetection and adopted the 2σ upper limit. Such limits were measured on the rms maps at the source locations using circular apertures of sizes equivalent to those of the `MAG_ISO` apertures.

---

[1] See https://github.com/mmechtley/astroRMS; we modified the routine slightly by adopting a better source masking functionality.

For simplicity, hereafter we denote the magnitudes in the HST/ACS F435W, F606W, F775W, F814W, and F850LP bands as m_{435}, m_{606}, m_{775}, m_{814}, and m_{850}, respectively, those in the JWST/NIRCam F090W, F115W, F150W, F200W, F277W, F335M, F356W, F410M, and F444W bands as m_{090}, m_{115}, m_{150}, m_{200}, m_{277}, m_{335}, m_{356}, m_{410}, and m_{444}, respectively, and those in the JWST/MIRI F560W, F770W, F1000W, F1280W, F1500W, F1800W, F2100W, and F2550W as m_{560}, m_{770}, m_{1000}, m_{1280}, m_{1500}, m_{1800}, m_{2100}, and m_{2550}, respectively.

4. Selection of Very Bright Dropouts

As mentioned in Section 3.1, the dropout selection was done using the NIRCam photometry based on the non-PSF-matched images. This approach has multiple advantages over using the PSF-matched images, such as no artificially introduced blending problem, less chance of misidentifying a broadened artifact as a source, more accurate S/N assessment, etc. The potential caveat of biased color indices using non-PSF-matched images has only a marginal impact here for two reasons. First, our objects would be dropouts from the bands bluer than F356W (the vast majority being dropouts from the SW bands), and the `MAG_ISO` aperture defined in F356W is large enough to include most (if not all) of the light in these bands in the first place. Second, the break amplitude is determined by the magnitudes in two adjacent bands whose PSF sizes are close, and the small difference in the fraction of light enclosed by the adopted aperture would only smear the redshift selection function negligibly.

Similar to H. Yan et al. (2023a, 2023b), we adopted the dropout selection criteria as follows.

(1) *S/N $\geqslant$ 5 in the shift-in band.* The shift-in band is the redder band adjacent to the dropout band. This criterion is to ensure the detection in the shift-in band and the robustness of the measured dropout amplitude.

(2) *Dropout amplitude $\geqslant$ 0.8 mag.* The dropout amplitude is the color index between the dropout and the shift-in bands. As mentioned above, when a source has S/N < 2 in the dropout band, its magnitude is substituted with the 2σ upper limit. This amplitude is chosen because the Lyman-break signature shifted halfway out of the dropout band would create a color index of ~ 0.75 mag between the dropout and shift-in bands for a flat spectrum in f_ν.

(3) *S/N $\geqslant$ 5 in at least one more band redder than the shift-in band.* All the retained sources have S/N $\geqslant$ 5 in F356W and the shift-in band, and this additional requirement further ensures the reliability of the detections.

(4) *S/N < 2 in all bands bluer than the dropout band.* A legitimate candidate should not be detected in these "veto" bands. This is the most important criterion that distinguishes the dropout selection and the ERO selection, whereas the latter does not have such a requirement.

The candidates thus selected were then visually examined in all bands to ensure that they are real sources and are indeed invisible in the veto bands. In this work, we only study very bright F090W and F115W dropouts with $m_{356} \leqslant 25.1$ mag and F150W, F200W, and F277W dropouts with $m_{356} \leqslant 26.0$ mag. The objects fainter than these limits are considered "normal" and are discussed in H. Yan et al. (2023b) (for the F150W, F200W and F277W dropouts) and in B. Sun & H. Yan (2025, in preparation, for the F090W and F115W dropouts), respectively. In total, we have found 300 bright dropouts,
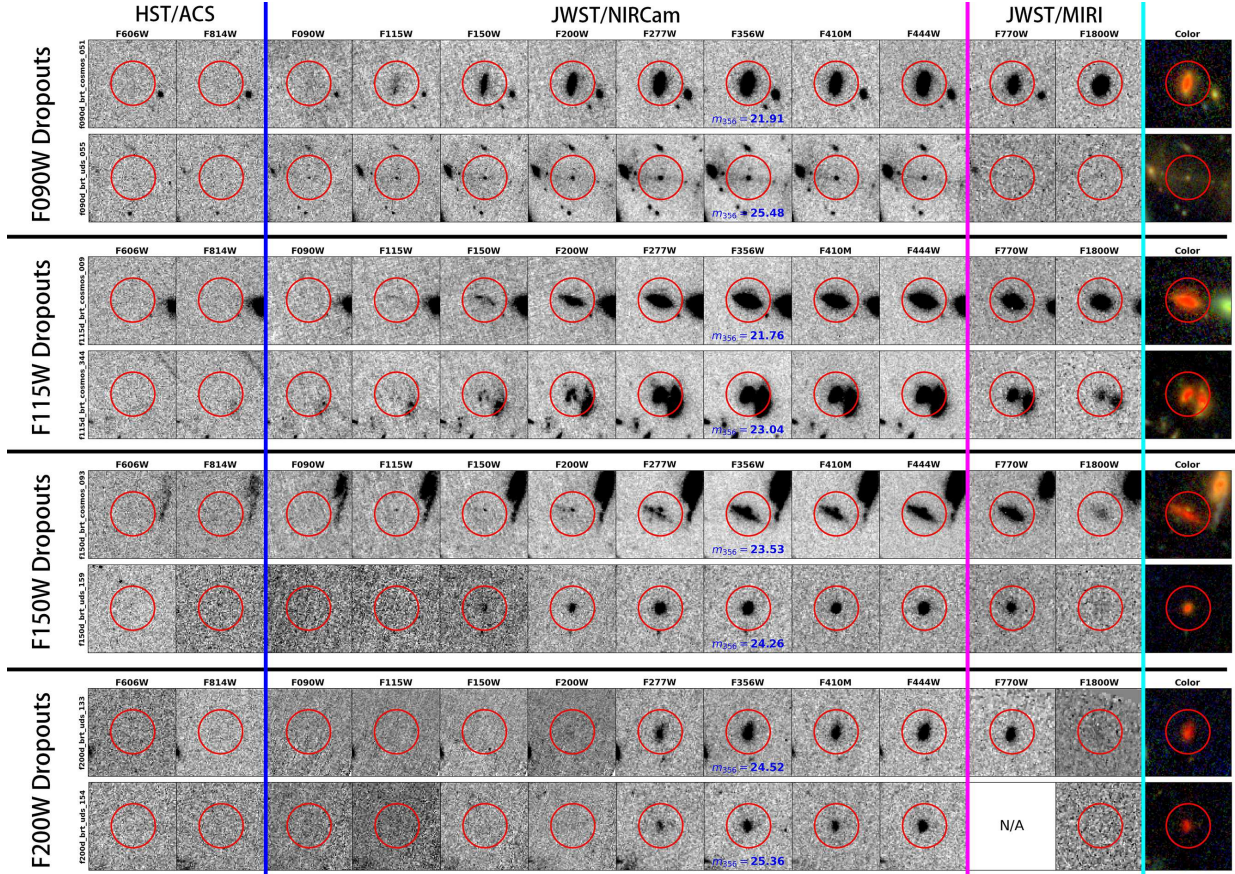
Figure 1. Image stamps of example very bright dropouts in F090W, F115W, F150W, and F200W, arranged from top to bottom. Two example objects are shown for each group. The stamps are $2'' \times 2''$ in size and are oriented with north being up and east being left. The images are from the HST ACS, JWST NIRCam, and JWST MIRI, with the passbands as noted. Most of the very bright dropouts are either disk-like ($\sim$40%) or compact ($\sim$45%) in morphology in F356W, and one each is shown for the F090W, F150W and F200W dropouts. The example F115W dropouts include a disk-like object and an irregular object. Only $\sim$15% of the very bright dropouts have irregular morphologies. The color stamps in the last column are constructed based on the NIRCam images, using F090W + F115W + F150W as blue, F200W + F277W as green, and F356W + F410M + F444W as red.

137 of which are covered by at least one MIRI band. We focus on these 137 dropouts that have MIRI photometry (with detections or upper limits), which form our main sample and will be discussed next. The other 163 objects form the supplement sample; for the sake of completeness, these objects are listed in Table A1. In the main sample, there are 59 dropouts in F090W, 36 in F115W, 37 in F150W, five in F200W, and none in F277W. Figure 1 shows the image stamps of two objects in each group as examples. The number of objects in the main sample in each field and each passband are listed in Table 3. If the dropout effect is due to the Lyman break, the nominal redshift ranges of the dropouts in F090W, F115W, F150W, and F200W are $z \approx 6.4$–8.4, 8.4–11.3, 11.3–15.4, and 15.4–21.8, respectively. The aforementioned brightness criteria roughly correspond to $M \lesssim -22$ mag in rest-frame U and B bands, respectively.

Moreover, we assessed the morphology of each source by visual inspection of the NIRCam images. Interestingly, most of these objects are either very compact or have disk-like morphology. Out of the 300 bright dropouts, $\sim$48% are compact sources, $\sim$38% are disk-like, $\sim$2% are elliptical, and $\sim$12% are irregular in shape. In the pre-JWST era, one would put the disk-like objects to low redshifts because common wisdom had been that disk galaxies cannot be formed so early in time. However, the JWST observations over the past two years have found a large number of candidate stellar disks at

$z > 2$ and up to $z \approx 8$ (e.g., L. Ferreira et al. 2022, 2023; Y. Fudamoto et al. 2022; C. Jacobs et al. 2023; E. J. Nelson et al. 2023; B. E. Robertson et al. 2023; V. Kuhn et al. 2024; H. Yan et al. 2024), which suggests an early formation of stellar disks. Therefore, we chose not to make the judgment based on morphology, and all objects were analyzed in the same way.

To demonstrate how the bright dropouts are qualified as EROs, Figure 2 shows the $m_{115} - m_{356}$ color distribution as a function of m_{356} for the 137 objects in our main sample, using different symbols for the dropouts from different bands. Even when adopting a very red color of $m_{115} - m_{356} > 2.0$ mag as the fiducial criterion for EROs, the vast majority (81%) of our bright dropouts would be selected.

5. SED Analysis

To better understand the nature of these bright dropouts, we analyzed the SEDs of the objects in the main sample. The SEDs were constructed using the photometry in both NIRCam and MIRI as detailed in Section 3.2, which was tailored for this purpose. Following the usual practice, we added 0.05 mag in quadrature to the reported photometric errors to account for the possible systematics, e.g., the offsets between the NIRCam and the MIRI photometry due to the different adopted methods.

Table 3
Statistics of Very Bright Dropouts in Each Field

Dropout Band	F090W	F115W	F150W	F200W	F277W	Total
COSMOS	29 (69)	10 (16)	15 (24)	1 (1)	0	55 (110)
High-z T1/T2	0/1	0/1	2/0	0/0	0	2/2
Low-z T1/T2	7/11	2/5	7/3	0/1	0	16/20
Undecided	10	2	3	0	0	15
UDS	21 (27)	20 (49)	17 (35)	4 (7)	0	62 (118)
High-z T1/T2	0/0	0/4	0/0	0/0	0	0/4
Low-z T1/T2	10/7	5/9	9/5	0/2	0	24/23
Undecided	4	2	3	2	0	11
CEERS	/	6 (37)	5 (13)	0 (2)	0	11 (52)
High-z T1/T2	/	0/1	1/0	0	0	1/1
Low-z T1/T2	/	2/2	0/2	0	0	2/4
Undecided	/	1	2	0	0	3
GOODS-S	9 (12)	0 (1)	0 (6)	0 (1)	0	9 (20)
High-z T1/T2	0/0	0/0	0	0	0	0/0
Low-z T1/T2	1/3	0/0	0	0	0	1/3
Undecided	5	0	0	0	0	5
Total	59 (108)	36 (103)	37 (78)	5 (11)	0	137 (300)

Note. For each field, the first row gives the total numbers of bright dropouts in the main sample (i.e., objects covered by at least one MIRI band), with the numbers in parentheses representing the total in the whole sample. The second and the third rows show the numbers of "high-z" and "low-z" objects in T1 and T2 (separated by "/"), respectively. The fourth row is the number of "undecided" objects. See Section 5.2 for details.

Figure 2. Observed $m_{115} - m_{356}$ color vs. m_{356} of the very bright dropouts in the main sample. The F090W, F115W, F150W, and F200W dropouts are represented by circles, squares, triangles, and stars, respectively. The ones with upward arrows indicate the lower limits of the color if the objects have S/N < 2.0 in F115W, and the color lower limits are calculated using the 2σ detection upper limits in this band. Adopting $m_{115} - m_{356} > 2.0$ mag as the fiducial criterion for EROs, the vast majority (81%)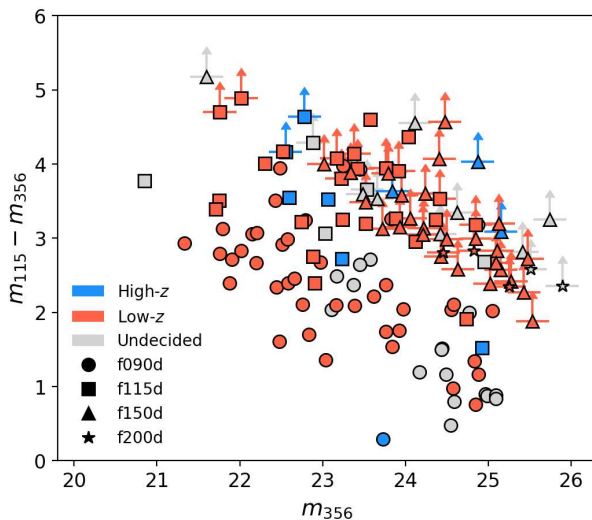 of the very bright dropouts shown here would be selected. The objects in the "high-z," "low-z," and "undecided" categories (see Section 5.2 for details) are shown in blue, red, and gray, respectively.

5.1. Methods and Procedures

We fitted the SEDs using three different tools, namely, Le Phare (version 2.2; S. Arnouts et al. 1999; O. Ilbert et al. 2006), EAZY (eazy-py version 0.6.4; G. B. Brammer et al. 2008), and CIGALE (version 2022.1; M. Boquien et al. 2019). A major goal was to obtain their photometric redshifts (z_{phot}),

which were allowed to vary between $z = 0$ to 25 in the fitting process. The settings for each tool are as follows.

1. *Le Phare*. We constructed the templates using the population synthesis models of G. Bruzual & S. Charlot (2003, hereafter "BC03") and the initial mass function (IMF) of G. Chabrier (2003). We adopted an exponentially declining star formation history, i.e., star formation rate (SFR) $\propto e^{-t/\tau}$, where τ ranges from 0 to 13 Gyr. We applied Calzetti's extinction law (D. Calzetti et al. 1994; D. Calzetti 2001) with $E(B-V)$ ranging from 0 to 1 mag at a step size of 0.1 mag. The option to include the contribution from emission lines was turned on.

2. *EAZY*. We used the template set GALSEDATLAS of M. J. I. Brown et al. (2014), which was retrieved from MAST. [2] This set includes the spectra of 129 nearby galaxies of different types, which cover the UV-to-mid-IR wavelength range. Presumably, using this set of templates would favor the fitting at low redshifts. We note that we did not use the template sets optimized for fitting $z \gtrsim 8$ galaxies (e.g., R. L. Larson et al. 2023a). Given the expectation that a significant fraction of the brightest dropouts would be EROs at low redshifts, using the GALSEDATLAS templates helps exclude high-z false positives as rigorously as possible.

3. *CIGALE*. We adopted a grid of CIGALE templates that include those using a delayed τ model in the form of SFR $\propto t e^{-t/\tau}$ with $0.01 < \tau \leqslant 13$ Gyr, a recent starburst, and the simple stellar population models (i.e., single bursts) from BC03 assuming Chabrier IMF; we fixed the metallicity to $Z = 0.02$. We set the nebular emission contribution with $-4 < \log U < -1$ at a step size of 0.5. We also adopted a modified Calzetti's extinction law under the dust_modified_starburst module

---

2 https://archive.stsci.edu/hlsp/galsedatlas
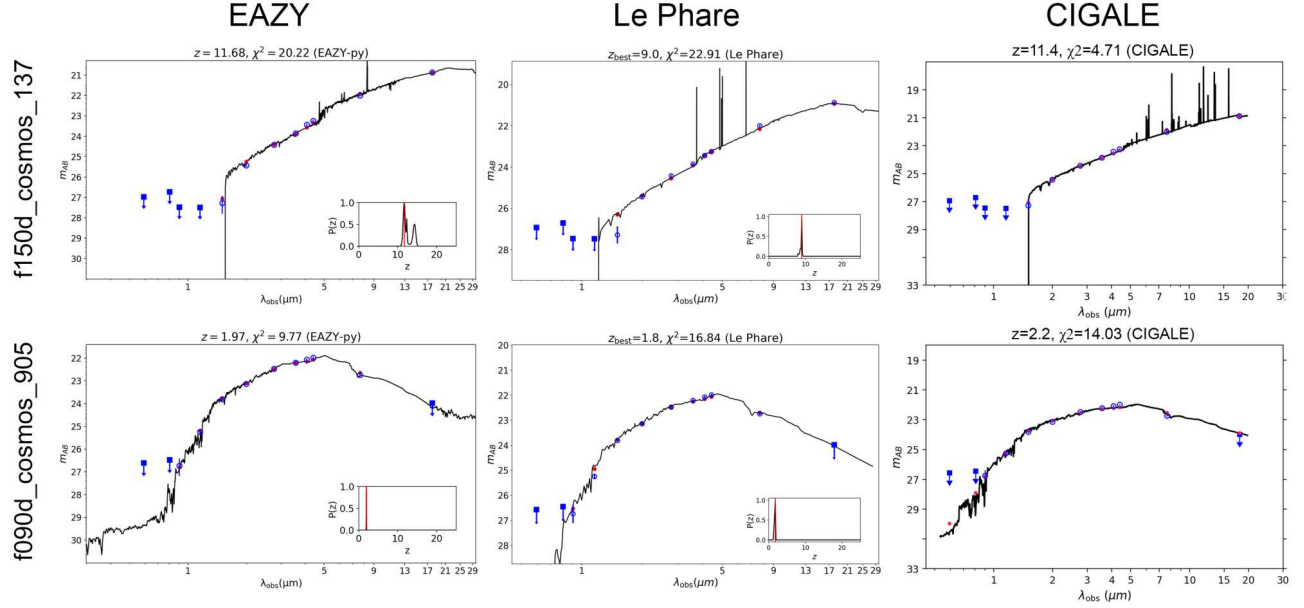
Figure 3. Examples of SED fitting results on one object in the "high-z" category (top panel) and one in the "low-z" category (bottom panel). The blue symbols represent the observed values, and the curves are the spectra of the best-fit models. The red symbols are the synthesized magnitudes derived from the best-fit models. The insets show the probability distribution function of z_{phot}. The quoted z_{phot} value on top of each panel is from the shown best-fit model, which is slightly different from the adopted value (see Table 4 for further explanation.)

with the color excess of nebular gas $E(B-V)_g$ ranging from 0 to 3 mag at a step of 0.2 mag, and a fixed multiplication factor of 0.44 to apply on $E(B-V)_g$ to calculate the stellar continuum attenuation $E(B-V)_s$. There are a lot of cases where the bright dropouts have enhanced emission in the central region increasing with wavelength, which could be caused by active galactic nuclei (AGNs). To investigate this probability, we included the `skirtor2016` AGN models from M. Stalevski et al. (2012, 2016). We varied the AGN fraction (hereafter f_{AGN}), i.e., the AGN contribution to L_{IR}, from 0 to 1 at a step size of 0.2. We set the viewing angles at either $30°$ or $70°$ for Type 1 or 2 AGNs, respectively. We noticed that the program would run into errors when $f_{AGN} = 1$, and we resolved this by setting the maximum f_{AGN} to 0.999[3] For the objects that do not show a compact central region at any passbands (in other words, their optical-to-IR emission is not likely due to AGN), we fixed their $f_{AGN} = 0$. Examples of SED fitting results from these three runs are provided in Figure 3. We note on the treatment of the upper limits. For Le Phare, we set the magnitude error to -1 when a given band has the upper limit imposed, and the routine rejected any fits that violated the upper limit. For EAZY, we used the modified code as described in H. Yan et al. (2023a, 2023b) to achieve this functionality. For CIGALE, we set the fluxes to the upper limit and the corresponding flux errors to -1 times the upper limit.

5.2. Categorizing Bright Dropouts

We divided the bright dropouts in the main sample into three categories based on their z_{phot}, namely, "high-z," "low-z," and "undecided." The "high-z" category consists of objects for

which at least two SED fitting tools (among the three) consistently derive $z_{phot} \geqslant 6.0$. Similarly, the "low-z" category consists of objects with consistent $z_{phot} < 6.0$ from at least two fitting tools. In both categories, we further ranked the objects into "Tier 1" (T1) and "Tier 2" (T2) depending on the goodness of fits and the consistency of the results. For practical purposes, we deemed the fits with raw $\chi^2 \leqslant 100$ as "good" fits. For the "high-z" category, if an object has good fits and $z_{phot} \geqslant 6.0$ from all three tools, it was put in T1; if it has good fits and $z_{phot} \geqslant 6.0$ from only two tools, or if it has $z_{phot} \geqslant 6.0$ from all three tools but the fits are not always good, it was placed in T2. The ranking for the "low-z" category was done similarly, with a slightly more stringent requirement on the consistency of z_{phot}: if an object has good fits and consistent z_{phot} from all three tools so that the differences $\Delta z_{phot} < 1.0$, it was put in T1; if it has good fits and consistent z_{phot} from only two tools, or if it has consistent z_{phot} from all three tools but the fits are not always good, it was placed in T2. Finally, all objects that were not in either the "high-z" or the "low-z" category as ranked were assigned to the "undecided" category.

1. *High-z*. We identified 10 high-z candidates from the sample, among which three are in T1 and seven are in T2. They are listed in Tables 4 and 5, respectively, along with their physical properties derived from the SED analysis.
2. *Low-z*. There are 43 T1 and 50 T2 objects in this category, which are listed in Tables 6 and 7, respectively. Among the 93 objects, the vast majority of them have $z_{phot} = 1$–4.
3. *Undecided*. This category contains 34 objects that cannot be placed in either of these categories. For the sake of completeness, they are listed in Table B1.

In the $m_{115} - m_{356}$ versus m_{356} distribution shown in Figure 2, the objects in the above three categories are indicated by different colors. It is obvious that many "high-z" objects

---

[3] In the cases of CIGALE returning $f_{AGN} = 0.999$, they are reported as $f_{AGN} = 1.0$.

Table 4
Tier 1 "High-z" Objects

SID	R.A.	Decl.	m_{in}	m_{356}	z_{lp}	z_{ez}	z_{cg}	$\log(M_*)$ $(M_\odot)$	f_{AGN}	$E(B-V)$	Age (Myr)	$\log(SFR)$ $(M_\odot\ yr^{-1})$	Morph
f150d_brt_ceers_051	215.0313294	52.9171141	26.57	24.89	$12.22^{+0.24}_{-0.28}$	$14.57^{+0.01}_{-0.01}$	$14.38^{+0.62}_{-0.73}$	$11.47^{+0.06}_{-0.09}/11.90^{+0.37}_{-11.90}$	$.../0.62^{+0.27}_{-0.27}$	$0.7/0.82^{+0.41}_{-0.26}$	$34^{+78}_{-19}/55^{+74}_{-55}$	$5.36^{+0.40}_{-0.51}/4.77^{+0.34}_{-4.77}$	c
f150d_brt_cosmos_093	150.0651062	2.2636221	27.60	23.53	$10.66^{+0.25}_{-0.23}$	$11.06^{+0.02}_{-0.02}$	$9.95^{+0.13}_{-0.18}$	$10.86^{+0.20}_{-0.05}/10.99^{+0.07}_{-0.08}$	$.../0$	$0.5/0.59^{+0.05}_{-0.05}$	$10^{+1}_{-1}/11^{+11}_{-11}$	$3.91^{+0.29}_{-0.11}/4.29^{+0.08}_{-0.09}$	d
f150d_brt_cosmos_137	150.1089402	2.2936631	25.49	23.86	$8.81^{+0.27}_{-0.53}$	$11.68^{+0.22}_{-0.22}$	$10.75^{+2.31}_{-2.31}$	$11.11^{+0.04}_{-0.05}/11.17^{+0.29}_{-1.17}$	$.../0.35^{+0.24}_{-0.24}$	$0.7/0.60^{+0.21}_{-0.21}$	$11^{+3}_{-1}/14^{+18}_{-14}$	$4.07^{+0.09}_{-0.07}/4.14^{+0.40}_{-4.14}$	c

Note. The brightness of an object is indicated using the shift in band magnitude (m_{in}) and m_{356}. The photometric redshifts from Le Phare, EAZY, and CIGALE are listed as z_{lp}, z_{ez}, and z_{cg}, respectively. The stellar mass (M_*), reddening ($E(B-V)$) and SFR estimates are from the Le Phare and the CIGALE runs but are not available in the EAZY runs, and therefore only two sets of values are quoted (separated by "/"). The AGN fraction (f_{AGN}) estimates are only available from CIGALE. For Le Phare and EAZY, the photometric redshifts are the mean values weighted by the probability distribution function $P(z)$. For CIGALE, z_{cg}, along with stellar mass, f_{AGN}, $E(B-V)$, Age, and SFR are all the 50th percentile values, and the errors indicate the 16th and 84th percentile values. The morphological classifications are given under the last column, where "c" stands for "compact" and "d" stands for "disk-like."

Table 5
Tier 2 "High-z" Objects

SID	R.A.	Decl.	m_{in}	m_{356}	z_{lp}	z_{ez}	z_{cg}	$\log(M_*)$ $(M_\odot)$	f_{AGN}	$E(B-V)$	Age (Myr)	$\log(SFR)$ $(M_\odot\,yr^{-1})$	Morph
f115d_brt_ceers_062	215.0354323	52.8906847	24.95	24.92	$8.80^{+0.14}_{-0.14}$	$8.88^{+0.01}_{-0.01}$	$8.95^{+0.12}_{-0.12}$	$9.26^{+0.04}_{-0.04}/8.94^{+0.09}_{-0.11}$	$.../0.32^{+0.29}_{-0.29}$	$0.2/0.09^{+0.02}_{-0.02}$	$11^{+3}_{-1}/15^{+44}_{-15}$	$2.60^{+0.08}_{-0.07}/2.19^{+0.09}_{-0.09}$	c
f090d_brt_cosmos_663	150.0634749	2.3552383	24.03	23.56	$6.16^{+0.16}_{-0.16}$	$6.88^{+0.00}_{-0.00}$	$6.78^{+0.09}_{-0.09}$	$-/9.04^{+0.09}_{-0.11}$	$-/0.43^{+0.36}_{-0.36}$	$-/0.01^{+0.03}_{-0.01}$	$-/21^{+12}_{-12}$	$-/2.11^{+0.11}_{-0.11}$	c
f115d_brt_cosmos_270	150.0985778	2.3208768	25.45	22.75	$7.93^{+0.20}_{-0.83}$	$6.70^{+0.01}_{-0.01}$	$2.86^{+0.78}_{-0.78}$	$11.50^{+0.05}_{-0.09}/-$	$.../-$	$0.7/-$	$111^{+10}_{-8}/-$	$4.81^{+0.09}_{-0.18}/-$	d
f115d_brt_uds_089	34.2669263	−5.2947891	25.05	23.25	$8.37^{+0.23}_{-0.28}$	$2.64^{+0.07}_{-0.07}$	$7.62^{+1.15}_{-1.15}$	$10.76^{+0.04}_{-0.05}/10.69^{+0.26}_{-0.75}$	$.../0.44^{+0.29}_{-0.29}$	$0.5/0.52^{+0.23}_{-0.23}$	$12^{+1}_{-2}/257^{+327}_{-257}$	$3.69^{+0.08}_{-0.08}/3.09^{+0.52}_{-3.09}$	c
f115d_brt_uds_245	34.4716256	−5.256956	24.38	22.62	$8.78^{+0.15}_{-0.14}$	$2.46^{+0.02}_{-0.02}$	$8.55^{+1.47}_{-1.47}$	$10.99^{+0.04}_{-0.03}/10.49^{+0.41}_{-10.49}$	$.../0.72^{+0.23}_{-0.23}$	$0.5/0.48^{+0.34}_{-0.34}$	$10^{+1}_{-1}/166^{+225}_{-166}$	$4.04^{+0.08}_{-0.09}/2.50^{+0.49}_{-2.50}$	irr
f115d_brt_uds_647	34.2421684	−5.1472847	25.06	23.06	$8.66^{+0.17}_{-0.20}$	$2.54^{+0.02}_{-0.02}$	$7.54^{+2.24}_{-2.24}$	$10.80^{+0.04}_{-0.04}/10.74^{+0.15}_{-0.24}$	$.../0$	$0.5/0.54^{+0.06}_{-0.06}$	$10^{+1}_{-1}/160^{+476}_{-160}$	$3.79^{+0.07}_{-0.07}/3.98^{+0.17}_{-0.27}$	c
f115d_brt_uds_754	34.3546998	−5.1097457	24.96	22.57	$5.60^{+0.14}_{-0.14}$	$9.27^{+0.06}_{-0.02}$	$9.91^{+1.84}_{-1.84}$	$11.17^{+0.08}_{-0.05}/11.52^{+0.17}_{-0.27}$	$.../0$	$0.9/0.60^{+0.09}_{-0.09}$	$10^{+1}_{-1}/27^{+84}_{-27}$	$4.12^{+0.07}_{-0.09}/4.65^{+0.19}_{-0.34}$	irr

Note. Similar to Table 4 but for the Tier 2 objects in the "high-z" category. Some of the parameters derived by Le Phare are not available because of the very bad fits. The redshift solution by CIGALE for f115d_brt_cosmos_270 is inconsistent with the other two tools, and its derived parameters are therefore not included for comparison. The morphological type "irr" stands for "irregular."
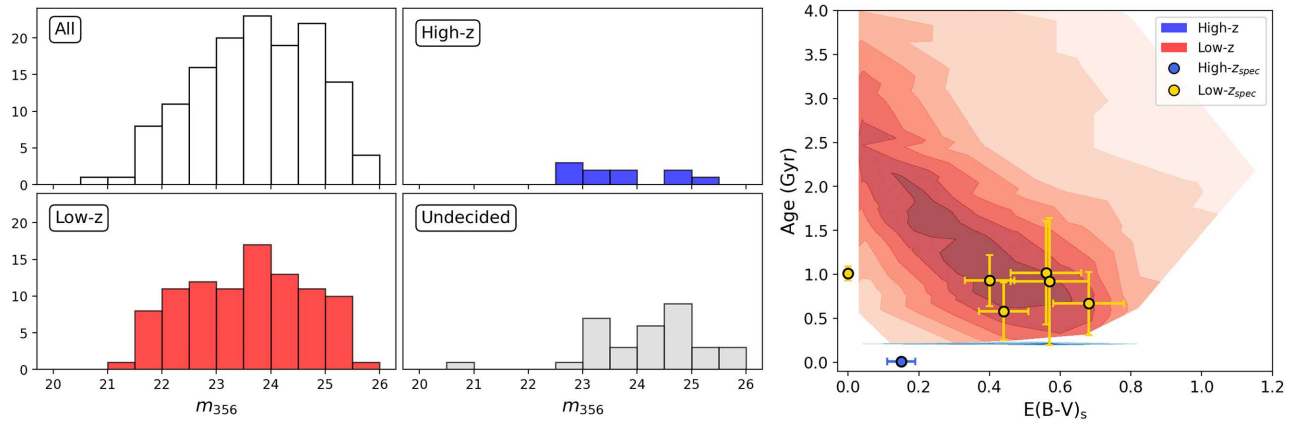
Table 6
Tier 1 "Low-z" Objects

SID	R.A.	Decl.	m_{in}	m_{356}	z_{lp}	z_{ez}	z_{cg}	$\log(M_*)$ ($M_\odot$)	f_{AGN}	$E(B-V)$	Age (Gyr)	$\log(SFR)$ ($M_\odot$ yr^{-1})	Morph
f115d_brt_ceers_146	215.041352	52.914094	25.16	22.53	$1.80^{+0.15}_{-0.15}$	$2.64^{+0.06}_{-0.06}$	$1.69^{+0.32}_{-0.41}$	$10.49^{+0.08}_{-0.11}/10.54^{+0.01}_{-0.06}$	$.../0$	$0.6/0.68^{+0.21}_{-0.18}$	$1.60^{+0.59}_{-0.75}/1.56^{+1.47}_{-0.85}$	$0.88^{+0.35}_{-0.19}/-11.53^{+10.98}_{-34.29}$	d
f115d_brt_ceers_309	214.9785887	52.9215485	24.88	23.29	$2.62^{+0.14}_{-0.15}$	$2.40^{+0.07}_{-0.07}$	$2.50^{+0.30}_{-0.47}$	$10.29^{+0.04}_{-0.04}/10.29^{+0.01}_{-0.03}$	$.../0.21^{+0.24}_{-0.21}$	$0.0/0.06^{+0.11}_{-0.05}$	$1.77^{+0.18}_{-0.18}/1.76^{+0.82}_{-0.71}$	$-4.77^{+2.77}_{-0.83}/-38.01^{+24.91}_{-23.87}$	c
f090d_brt_cosmos_296	150.0880207	2.2795606	25.84	23.64	$1.46^{+0.15}_{-0.17}$	$1.61^{+0.03}_{-0.03}$	$1.62^{+0.21}_{-0.22}$	$9.83^{+0.05}_{-0.05}/9.86^{+0.01}_{-0.01}$	$.../0$	$0.1/0.04^{+0.05}_{-0.03}$	$3.78^{+0.67}_{-0.59}/3.26^{+0.42}_{-0.33}$	$-3.16^{+1.26}_{-1.64}/-26.62^{+24.99}_{-74.26}$	e
f090d_brt_cosmos_364	150.0869802	2.289832	24.85	22.02	$1.78^{+0.15}_{-0.17}$	$1.60^{+0.01}_{-0.01}$	$1.24^{+0.19}_{-0.16}$	$-/10.16^{+0.01}_{-0.01}$	$.../0$	$0.6/0.61^{+0.04}_{-0.04}$	$-/3.34^{+1.04}_{-1.05}$	$-/0.89^{+0.01}_{-0.01}$	irr
f090d_brt_cosmos_543	150.1822751	2.3270705	26.04	22.80	$2.54^{+0.17}_{-0.14}$	$2.41^{+0.02}_{-0.02}$	$2.48^{+0.24}_{-0.20}$	$10.55^{+0.07}_{-0.07}/10.54^{+0.01}_{-0.02}$	$.../0.44^{+0.35}_{-0.35}$	$0.0/0.04^{+0.05}_{-0.03}$	$1.78^{+0.18}_{-0.32}/2.06^{+0.60}_{-0.60}$	$-4.31^{+3.15}_{-1.18}/-43.07^{+28.54}_{-28.63}$	c
f090d_brt_cosmos_589	150.0687834	2.342366	26.05	24.97	$1.42^{+0.17}_{-0.19}$	$1.59^{+0.06}_{-0.06}$	$1.42^{+0.21}_{-0.19}$	$9.03^{+0.18}_{-0.53}/9.23^{+0.01}_{-0.01}$	$.../0$	$0.2/0.05^{+0.07}_{-0.05}$	$2.61^{+1.32}_{-2.48}/3.35^{+0.78}_{-0.49}$	$-0.38^{+0.49}_{-0.36}/-2.26^{+0.78}_{-90.99}$	c
f090d_brt_cosmos_653	150.0649198	2.3573118	25.55	24.64	$0.62^{+0.17}_{-0.16}$	$1.04^{+0.03}_{-0.03}$	$0.99^{+0.19}_{-0.16}$	$7.88^{+0.05}_{-0.06}/8.92^{+0.01}_{-0.01}$	$.../0$	$1.0/0.03^{+0.04}_{-0.03}$	$0.01^{+6.91}_{-0.00}/2.04^{+15.02}_{-0.32}$	$1.00^{+0.08}_{-0.09}/-17.26^{+15.02}_{-45.45}$	d
f090d_brt_cosmos_676	150.0844722	2.3576783	24.40	23.10	$1.20^{+0.15}_{-0.14}$	$1.13^{+0.04}_{-0.04}$	$0.99^{+0.18}_{-0.16}$	$9.78^{+0.10}_{-1.53}/9.65^{+0.01}_{-0.01}$	$.../0$	$0.0/0.03^{+0.04}_{-0.03}$	$4.65^{+0.72}_{-1.12}/3.80^{+1.05}_{-0.80}$	$2.83^{+6.91}_{-6.74}/-29.98^{+28.13}_{-88.00}$	c
f090d_brt_cosmos_905	150.1387124	2.4440275	25.28	22.21	$1.76^{+0.16}_{-0.15}$	$1.96^{+0.01}_{-0.01}$	$1.99^{+0.19}_{-0.15}$	$10.60^{+0.06}_{-0.06}/10.59^{+0.01}_{-0.01}$	$.../0.46^{+0.35}_{-0.35}$	$0.1/0.03^{+0.04}_{-0.03}$	$3.42^{+0.40}_{-0.31}/3.05^{+0.33}_{-0.46}$	$-5.05^{+2.33}_{-0.10}/-64.78^{+42.81}_{-43.85}$	c
f115d_brt_cosmos_086	150.0838418	2.236936	25.81	24.84	$1.41^{+0.14}_{-0.15}$	$1.34^{+0.02}_{-0.02}$	$1.21^{+0.21}_{-0.17}$	$9.15^{+0.13}_{-0.19}/9.17^{+0.01}_{-0.01}$	$.../0$	$0.0/0.04^{+0.05}_{-0.04}$	$4.80^{+0.51}_{-0.44}/3.96^{+0.57}_{-0.75}$	$2.83^{+0.07}_{-0.28}/-30.00^{+27.73}_{-92.46}$	c
f115d_brt_cosmos_226	150.1113201	2.2988013	25.90	24.13	$3.31^{+0.21}_{-0.22}$	$2.80^{+0.06}_{-0.06}$	$2.31^{+0.23}_{-0.22}$	$9.70^{+0.12}_{-0.13}/9.99^{+0.01}_{-0.01}$	$.../0$	$0.8/0.36^{+0.06}_{-0.07}$	$1.05^{+0.92}_{-0.45}/0.81^{+0.38}_{-0.39}$	$2.84^{+0.17}_{-0.15}/-6.12^{+5.36}_{-16.43}$	d
f150d_brt_cosmos_010	150.0949689	2.1771805	25.12	24.09	$3.11^{+0.27}_{-0.26}$	$3.03^{+0.07}_{-0.07}$	$3.41^{+0.30}_{-0.48}$	$9.90^{+0.15}_{-0.15}/10.16^{+0.03}_{-0.03}$	$.../0.40^{+0.35}_{-0.35}$	$1.0/0.05^{+0.04}_{-0.04}$	$2.84^{+0.18}_{-0.18}/1.36^{+0.56}_{-0.56}$	$3.22^{+0.15}_{-0.17}/-27.93^{+18.43}_{-18.05}$	c
f150d_brt_cosmos_044	150.0797437	2.2273521	26.24	25.04	$3.04^{+0.25}_{-0.22}$	$3.55^{+0.11}_{-0.11}$	$3.44^{+0.29}_{-0.30}$	$9.47^{+0.31}_{-0.23}/10.09^{+0.01}_{-0.03}$	$.../0$	$0.6/0.44^{+0.08}_{-0.09}$	$0.04^{+0.48}_{-0.03}/0.54^{+0.64}_{-0.46}$	$2.21^{+0.11}_{-0.86}/-0.42^{+0.99}_{-9.31}$	c
f150d_brt_cosmos_160	150.0817351	2.3043475	26.69	25.13	$1.71^{+0.19}_{-0.19}$	$2.43^{+0.05}_{-0.05}$	$1.52^{+0.42}_{-0.43}$	$8.72^{+0.59}_{-0.28}/9.46^{+0.02}_{-0.06}$	$.../0.14^{+0.20}_{-0.14}$	$0.8/0.77^{+0.21}_{-0.21}$	$0.07^{+1.24}_{-0.04}/2.43^{+1.04}_{-1.57}$	$0.83^{+0.28}_{-0.59}/0.03^{+0.09}_{-0.60}$	c
f150d_brt_cosmos_384	150.176541	2.4599094	26.24	25.37	$2.11^{+0.22}_{-0.22}$	$3.17^{+0.25}_{-0.25}$	$2.44^{+0.66}_{-0.16}$	$8.64^{+0.49}_{-0.12}/9.53^{+0.01}_{-0.01}$	$.../0$	$0.7/0.36^{+0.17}_{-0.17}$	$0.03^{+0.17}_{-0.02}/1.18^{+0.92}_{-0.51}$	$1.16^{+0.39}_{-0.45}/-8.06^{+6.83}_{-26.51}$	c
f150d_brt_cosmos_389	150.1539149	2.4671568	26.68	25.33	$3.40^{+0.31}_{-0.41}$	$3.64^{+0.19}_{-0.19}$	$3.74^{+0.31}_{-0.47}$	$9.39^{+0.24}_{-0.22}/9.97^{+0.02}_{-0.02}$	$.../0$	$0.9/0.25^{+0.09}_{-0.08}$	$1.20^{+0.67}_{-0.60}/0.91^{+0.51}_{-0.51}$	$2.47^{+0.30}_{-0.60}/-7.27^{+6.42}_{-18.37}$	c
f150d_brt_cosmos_390	150.1586059	2.4683481	25.14	24.00	$3.05^{+0.22}_{-0.20}$	$3.58^{+0.02}_{-0.02}$	$3.39^{+0.28}_{-0.27}$	$9.67^{+0.40}_{-0.13}/10.49^{+0.01}_{-0.02}$	$.../0$	$0.9/0.34^{+0.06}_{-0.08}$	$0.01^{+0.26}_{-0.00}/0.81^{+0.36}_{-0.36}$	$2.50^{+0.23}_{-0.76}/-2.53^{+3.28}_{-25.68}$	d
f150d_brt_cosmos_400	150.149107	2.4827173	24.99	24.23	$2.30^{+0.28}_{-0.27}$	$2.29^{+0.10}_{-0.10}$	$2.73^{+0.46}_{-0.56}$	$9.87^{+0.12}_{-0.68}/10.04^{+0.01}_{-0.03}$	$.../0.36^{+0.35}_{-0.35}$	$1.0/0.05^{+0.11}_{-0.05}$	$2.28^{+0.64}_{-0.68}/1.85^{+0.72}_{-0.72}$	$1.63^{+1.69}_{-3.14}/-38.80^{+25.42}_{-25.68}$	c
f090d_brt_jsmed_191	53.0471741	−27.8700154	27.22	22.83	$3.19^{+0.18}_{-0.18}$	$3.64^{+0.03}_{-0.03}$	$2.88^{+0.32}_{-0.32}$	$10.28^{+0.14}_{-0.07}/10.81^{+0.01}_{-0.01}$	$.../0$	$1.0/0.67^{+0.09}_{-0.10}$	$0.01^{+0.20}_{-0.00}/0.32^{+0.56}_{-0.30}$	$3.26^{+0.20}_{-0.21}/0.01^{+0.42}_{-5.69}$	irr
f090d_brt_uds_008	34.4023528	−5.2907091	25.26	23.20	$1.74^{+0.17}_{-0.18}$	$1.74^{+0.02}_{-0.02}$	$1.76^{+0.22}_{-0.20}$	$10.06^{+0.06}_{-0.06}/10.12^{+0.01}_{-0.01}$	$.../0.41^{+0.35}_{-0.35}$	$0.1/0.04^{+0.06}_{-0.04}$	$2.42^{+0.81}_{-0.67}/2.85^{+0.50}_{-0.82}$	$-0.32^{+0.26}_{-0.33}/-60.31^{+40.19}_{-40.49}$	c
f090d_brt_uds_020	34.4040888	−5.283555	24.87	22.23	$1.80^{+0.14}_{-0.14}$	$1.89^{+0.01}_{-0.01}$	$1.93^{+0.21}_{-0.16}$	$10.51^{+0.07}_{-2.05}/10.59^{+0.01}_{-0.01}$	$.../0.37^{+0.36}_{-0.36}$	$0.1/0.05^{+0.06}_{-0.04}$	$3.40^{+0.41}_{-0.39}/3.13^{+0.28}_{-0.37}$	$3.32^{+0.11}_{-5.99}/-67.46^{+45.00}_{-43.51}$	c
f090d_brt_uds_035	34.2395469	−5.2770455	26.13	23.77	$1.83^{+0.16}_{-0.16}$	$1.82^{+0.02}_{-0.02}$	$1.83^{+0.19}_{-0.15}$	$9.85^{+0.06}_{-0.08}/9.94^{+0.02}_{-0.01}$	$.../0.26^{+0.25}_{-0.25}$	$0.1/0.04^{+0.08}_{-0.04}$	$1.89^{+0.66}_{-0.66}/2.73^{+1.35}_{-0.82}$	$-1.88^{+0.93}_{-3.33}/-58.12^{+37.98}_{-38.26}$	c
f090d_brt_uds_038	34.3312534	−5.2762723	26.02	24.00	$1.80^{+0.15}_{-0.14}$	$2.10^{+0.02}_{-0.02}$	$1.78^{+0.26}_{-0.26}$	$9.62^{+0.08}_{-0.13}/9.76^{+0.04}_{-0.04}$	$.../0$	$0.4/0.19^{+0.09}_{-0.08}$	$1.21^{+0.66}_{-0.45}/1.53^{+1.35}_{-0.72}$	$0.46^{+0.16}_{-0.33}/-12.07^{+10.68}_{-33.76}$	irr
f090d_brt_uds_087	34.3935038	−5.2608125	25.48	23.45	$1.69^{+0.17}_{-0.17}$	$1.75^{+0.05}_{-0.05}$	$1.77^{+0.21}_{-0.20}$	$9.93^{+0.06}_{-0.07}/10.03^{+0.01}_{-0.01}$	$.../0.44^{+0.35}_{-0.35}$	$0.1/0.04^{+0.04}_{-0.04}$	$2.40^{+0.95}_{-0.54}/2.91^{+0.46}_{-0.54}$	$-2.22^{+5.08}_{-2.20}/-64.99^{+42.87}_{-40.37}$	c
f090d_brt_uds_261	34.2702143	−5.1423084	26.59	24.68	$1.49^{+0.17}_{-0.18}$	$1.49^{+0.01}_{-0.01}$	$1.39^{+0.22}_{-0.23}$	$9.33^{+0.09}_{-1.29}/9.27^{+0.01}_{-0.01}$	$.../0.45^{+0.35}_{-0.35}$	$0.0/0.04^{+0.05}_{-0.04}$	$4.02^{+0.52}_{-0.54}/3.56^{+0.63}_{-0.54}$	$2.96^{+0.16}_{-0.25}/-76.32^{+50.15}_{-50.79}$	c
f090d_brt_uds_289	34.3824186	−5.1345838	25.94	22.44	$2.39^{+0.14}_{-0.15}$	$2.46^{+0.01}_{-0.01}$	$2.43^{+0.24}_{-0.23}$	$10.71^{+0.07}_{-0.07}/10.74^{+0.01}_{-0.01}$	$.../0$	$0.1/0.14^{+0.07}_{-0.06}$	$2.14^{+0.28}_{-0.28}/2.12^{+0.55}_{-0.61}$	$-1.37^{+0.35}_{-1.00}/-16.48^{+15.67}_{-46.90}$	irr
f090d_brt_uds_296	34.4194596	−5.1337748	25.12	22.71	$1.84^{+0.16}_{-0.16}$	$2.10^{+0.04}_{-0.04}$	$1.81^{+0.21}_{-0.24}$	$10.21^{+0.05}_{-0.05}/10.35^{+0.01}_{-0.02}$	$.../0$	$0.4/0.20^{+0.06}_{-0.04}$	$0.59^{+0.71}_{-0.15}/2.14^{+0.99}_{-0.75}$	$0.30^{+0.25}_{-0.16}/-16.74^{+15.48}_{-46.87}$	c
f090d_brt_uds_310	34.5003733	−5.1291902	25.50	23.74	$1.16^{+0.17}_{-0.59}$	$1.25^{+0.01}_{-0.01}$	$1.08^{+0.17}_{-0.21}$	$8.91^{+0.41}_{-0.43}/9.47^{+0.01}_{-0.01}$	$.../0.49^{+0.34}_{-0.34}$	$0.0/0.03^{+0.04}_{-0.03}$	$6.25^{+1.68}_{-1.19}/4.09^{+0.80}_{-0.98}$	$2.17^{+0.53}_{-6.50}/-87.53^{+58.22}_{-59.46}$	c
f090d_brt_uds_339	34.3837744	−5.1194462	25.68	23.96	$1.68^{+0.16}_{-0.17}$	$1.64^{+0.05}_{-0.05}$	$1.26^{+0.23}_{-0.19}$	$9.70^{+0.09}_{-0.08}/9.48^{+0.01}_{-0.02}$	$.../0.36^{+0.31}_{-0.31}$	$0.1/0.22^{+0.08}_{-0.10}$	$2.21^{+1.16}_{-0.41}/1.84^{+1.65}_{-1.01}$	$-1.87^{+5.07}_{-1.56}/-39.05^{+24.95}_{-24.63}$	c
f115d_brt_uds_151	34.39082	−5.2791002	25.15	23.55	$1.71^{+0.25}_{-0.33}$	$2.46^{+0.01}_{-0.01}$	$2.44^{+0.22}_{-0.16}$	$9.29^{+0.13}_{-0.45}/9.26^{+0.01}_{-0.03}$	$.../0$	$0.6/0.03^{+0.04}_{-0.03}$	$0.08^{+0.20}_{-0.05}/2.47^{+0.34}_{-0.43}$	$2.13^{+0.14}_{-1.03}/-17.91^{+16.64}_{-36.50}$	d
f115d_brt_uds_265	34.3571218	−5.2531005	25.94	23.91	$2.88^{+0.18}_{-0.15}$	$3.03^{+0.03}_{-0.03}$	$2.73^{+0.26}_{-0.26}$	$10.05^{+0.10}_{-0.31}/10.30^{+0.01}_{-0.05}$	$.../0$	$0.5/0.19^{+0.07}_{-0.08}$	$0.10^{+0.58}_{-0.02}/1.59^{+0.61}_{-0.61}$	$1.22^{+1.45}_{-0.38}/-12.77^{+11.82}_{-33.83}$	e
f115d_brt_uds_685	34.3435201	−5.1347536	26.08	23.40	$3.17^{+0.17}_{-0.17}$	$3.41^{+0.06}_{-0.06}$	$2.66^{+0.32}_{-0.32}$	$10.61^{+0.14}_{-0.11}/10.62^{+0.01}_{-0.06}$	$.../0$	$1.0/0.69^{+0.06}_{-0.07}$	$0.41^{+0.66}_{-0.24}/0.47^{+0.60}_{-0.40}$	$1.93^{+0.23}_{-0.18}/-2.10^{+2.13}_{-8.64}$	e
f115d_brt_uds_739	34.2446999	−5.1153672	26.31	24.43	$2.75^{+0.21}_{-0.30}$	$2.96^{+0.08}_{-0.08}$	$2.57^{+0.38}_{-0.14}$	$9.46^{+0.10}_{-0.11}/10.01^{+0.01}_{-0.01}$	$.../0.06^{+0.15}_{-0.06}$	$0.8/0.34^{+0.14}_{-0.10}$	$0.03^{+0.02}_{-0.02}/1.07^{+0.86}_{-0.54}$	$2.57^{+0.91}_{-0.83}/-22.33^{+14.47}_{-14.78}$	c
f115d_brt_uds_813	34.3211879	−5.2680748	26.42	22.18	$2.26^{+0.15}_{-0.18}$	$2.77^{+0.04}_{-0.04}$	$2.04^{+0.36}_{-0.28}$	$10.79^{+0.10}_{-0.10}/10.78^{+0.01}_{-0.02}$	$.../0$	$0.5/0.61^{+0.18}_{-0.18}$	$1.10^{+0.14}_{-0.61}/0.78^{+0.27}_{-0.58}$	$1.63^{+0.14}_{-0.44}/-0.17^{+0.48}_{-19.16}$	irr
f150d_brt_uds_046	34.4382923	−5.2943129	25.16	23.55	$2.81^{+0.15}_{-0.16}$	$3.65^{+0.07}_{-0.07}$	$2.68^{+0.31}_{-0.28}$	$10.00^{+0.29}_{-0.38}/10.46^{+0.01}_{-0.02}$	$.../0$	$0.7/0.50^{+0.07}_{-0.10}$	$0.16^{+0.46}_{-0.14}/0.86^{+0.56}_{-0.46}$	$1.86^{+0.57}_{-0.30}/-0.50^{+0.27}_{-18.70}$	irr
f150d_brt_uds_069	34.3171538	−5.2855252	26.44	25.17	$2.84^{+0.14}_{-0.16}$	$3.57^{+0.04}_{-0.04}$	$2.97^{+0.28}_{-0.24}$	$9.08^{+0.11}_{-0.09}/9.95^{+0.07}_{-0.07}$	$.../0.02^{+0.09}_{-0.02}$	$0.8/0.28^{+0.10}_{-0.09}$	$0.03^{+0.03}_{-0.02}/1.51^{+0.56}_{-0.61}$	$1.63^{+0.30}_{-0.19}/-33.06^{+21.61}_{-21.19}$	c
f150d_brt_uds_090	34.3865074	−5.2751339	26.49	24.53	$3.28^{+0.20}_{-0.23}$	$3.88^{+0.01}_{-0.01}$	$3.23^{+0.30}_{-0.29}$	$9.81^{+0.09}_{-0.09}/10.48^{+0.01}_{-0.03}$	$.../0$	$0.8/0.65^{+0.09}_{-0.09}$	$0.04^{+0.10}_{-0.01}/0.67^{+0.47}_{-0.51}$	$2.21^{+0.15}_{-0.30}/-0.34^{+0.16}_{-14.54}$	d
f150d_brt_uds_143	34.404667	−5.2547906	25.38	24.69	$2.19^{+0.25}_{-0.25}$	$2.24^{+0.07}_{-0.07}$	$2.19^{+0.40}_{-0.31}$	$9.47^{+0.18}_{-0.51}/9.70^{+0.01}_{-0.02}$	$.../0.33^{+0.32}_{-0.32}$	$1.0/0.08^{+0.11}_{-0.07}$	$2.76^{+0.55}_{-0.70}/2.24^{+0.73}_{-0.55}$	$2.10^{+0.18}_{-4.02}/-48.63^{+31.52}_{-31.30}$	c
f150d_brt_uds_181	34.375762	−5.2418499	26.39	25.12	$2.81^{+0.14}_{-0.14}$	$3.04^{+0.03}_{-0.03}$	$3.17^{+0.32}_{-0.28}$	$9.53^{+0.21}_{-0.28}/10.14^{+0.01}_{-0.03}$	$.../0.02^{+0.06}_{-0.02}$	$0.7/0.55^{+0.10}_{-0.11}$	$0.08^{+0.13}_{-0.03}/0.73^{+0.64}_{-0.56}$	$1.75^{+0.34}_{-0.58}/-0.08^{+0.10}_{-16.02}$	c
f150d_brt_uds_334	34.3821957	−5.1538846	26.07	24.88	$3.19^{+0.20}_{-0.20}$	$3.34^{+0.05}_{-0.05}$	$2.92^{+0.35}_{-0.34}$	$9.54^{+0.31}_{-0.31}/10.03^{+0.03}_{-0.03}$	$.../0.08^{+0.15}_{-0.08}$	$0.8/0.43^{+0.11}_{-0.11}$	$0.12^{+0.15}_{-0.05}/0.76^{+0.74}_{-0.56}$	$2.01^{+0.44}_{-0.58}/-0.28^{+0.09}_{-16}$	c
f150d_brt_uds_345	34.5014752	−5.1511903	25.27	24.02	$2.21^{+0.15}_{-0.15}$	$2.91^{+0.05}_{-0.05}$	$2.61^{+0.36}_{-0.32}$	$9.51^{+0.40}_{-0.35}/10.26^{+0.01}_{-0.03}$	$.../0.06^{+0.14}_{-0.06}$	$0.7/0.30^{+0.11}_{-0.11}$	$0.23^{+0.28}_{-0.21}/1.71^{+0.66}_{-0.79}$	$1.72^{+1.44}_{-0.64}/-36.93^{+24.45}_{-23.64}$	c
f150d_brt_uds_346	34.4177096	−5.1495225	25.47	23.80	$3.24^{+0.19}_{-0.20}$	$3.78^{+0.01}_{-0.01}$	$3.11^{+0.35}_{-0.26}$	$10.12^{+0.34}_{-0.18}/10.68^{+0.01}_{-0.04}$	$.../0$	$0.8/0.66^{+0.09}_{-0.10}$	$0.05^{+0.19}_{-0.05}/0.50^{+0.62}_{-0.43}$	$2.36^{+0.21}_{-0.30}/0.17^{+1.02}_{-8.13}$	d
f150d_brt_uds_427	34.3320032	−5.1041668	25.83	24.49	$2.77^{+0.21}_{-0.18}$	$3.65^{+0.07}_{-0.07}$	$2.97^{+0.52}_{-0.36}$	$9.56^{+0.43}_{-0.28}/10.10^{+0.01}_{-0.02}$	$.../0.06^{+0.12}_{-0.06}$	$0.6/0.36^{+0.13}_{-0.13}$	$0.07^{+0.94}_{-0.05}/1.08^{+0.73}_{-0.54}$	$1.91^{+1.22}_{-0.69}/-23.00^{+14.95}_{-14.55}$	c

Note. Similar to Tables 4 and 5 but for the Tier 1 objects in the "low-z" category. In CIGALE, the stellar masses are the values rederived by rerunning it with the three parameters above fixed at their 50th percentile; this procedure is different from that of the CIGALE run for the objects in the "high-z" category, where the routine was run for only once and the stellar masses were obtained together with other parameters. The morphological type "e" stands for "elliptical."

Table 7
Tier 2 "Low-z" Objects

SID	R.A.	Decl.	m_{in}	m_{356}	z_{lp}	z_{ez}	z_{cg}	$\log(M_*)$ ($M_\odot$)	f_{AGN}	$E(B-V)$	Age (Gyr)	$\log(\mathrm{SFR})$ ($M_\odot\,\mathrm{yr}^{-1}$)	Morph
f115d_brt_ceers_246	214.8402602	52.8011294	26.00	24.55	$2.41^{+0.25}_{-0.24}$	$2.32^{+0.06}_{-0.06}$	$2.41^{+0.24}_{-0.24}$	$9.00^{+0.10}_{-0.07}/9.80^{+0.01}_{-0.04}$	$\ldots/0$	$0.9/0.21^{+0.07}_{-0.07}$	$0.01^{+0.01}_{-0.01}/1.70^{+0.83}_{-0.80}$	$1.95^{+0.19}_{-0.27}/-13.99^{+12.54}_{-37.18}$	c
f115d_brt_ceers_279	214.9417737	52.8845789	25.98	24.06	$1.14^{+0.17}_{-0.14}$	$2.64^{+0.06}_{-0.06}$	$0.95^{+0.22}_{-0.17}$	$9.66^{+0.11}_{-0.15}/9.52^{+0.01}_{-0.02}$	$\ldots/0.06^{+0.12}_{-0.06}$	$0.6/0.80^{+0.17}_{-0.13}$	$3.82^{+1.22}_{-1.30}/3.91^{+1.03}_{-1.02}$	$-0.67^{+0.44}_{-0.24}/-64.98^{+63.25}_{-69.99}$	c
f150d_brt_ceers_078	214.7713801	52.7497666	26.31	24.49	$3.26^{+0.28}_{-0.26}$	$3.95^{+0.06}_{-0.06}$	$1.30^{+12.30}_{-0.27}$	$10.43^{+0.05}_{-0.06}/-$	$\ldots/-$	$0.3/-$	$1.75^{+0.22}_{-0.29}/-$	$2.52^{+0.14}_{-2.07}/-$	c
f150d_brt_ceers_165	214.7680323	52.8164203	26.15	23.37	$2.80^{+0.14}_{-0.14}$	$3.39^{+0.37}_{-0.48}$	$3.32^{+0.30}_{-0.46}$	$10.60^{+0.04}_{-0.04}/10.58^{+0.01}_{-0.01}$	$\ldots/0$	$0.5/0.17^{+0.14}_{-0.06}$	$0.54^{+0.07}_{-0.20}/1.28^{+0.40}_{-0.46}$	$0.64^{+0.12}_{-2.16}/-9.30^{+8.79}_{-27.47}$	irr
f090d_brt_cosmos_013	150.0930808	2.1753794	24.79	22.46	$1.68^{+0.16}_{-0.18}$	$1.68^{+0.03}_{-0.03}$	$1.16^{+0.12}_{-0.17}$	$10.41^{+0.06}_{-0.06}/10.13^{+0.01}_{-0.01}$	$\ldots/0$	$0.2/0.30^{+0.06}_{-0.05}$	$3.33^{+0.51}_{-0.67}/3.11^{+0.39}_{-0.61}$	$-0.79^{+4.53}_{-2.46}/-23.69^{+22.22}_{-72.91}$	d
f090d_brt_cosmos_051	150.0811983	2.1939242	24.62	21.91	$1.97^{+5.89}_{-0.27}$	$2.01^{+0.00}_{-0.00}$	$1.24^{+0.19}_{-0.15}$	$-/10.17^{+0.01}_{-0.01}$	$\ldots/0$	$0.6/0.62^{+0.05}_{-0.04}$	$-/1.59^{+2.02}_{-1.19}$	$-/-0.86^{+0.01}_{-0.01}$	d
f090d_brt_cosmos_099	150.0747367	2.2164983	24.56	21.76	$7.00^{+0.14}_{-0.14}$	$2.08^{+0.00}_{-0.00}$	$1.82^{+0.27}_{-0.38}$	$-/10.68^{+0.01}_{-0.01}$	$\ldots/0$	$-/0.68^{+0.10}_{-0.08}$	$-/0.60^{+1.99}_{-0.53}$	$-/-1.03^{+0.02}_{-0.02}$	d
f090d_brt_cosmos_118	150.1026692	2.2248794	26.18	24.92	$5.57^{+0.18}_{-4.29}$	$1.20^{+0.15}_{-0.15}$	$1.01^{+0.19}_{-0.17}$	$9.12^{+0.13}_{-0.05}/8.88^{+0.01}_{-0.01}$	$\ldots/0$	$0.4/0.12^{+0.06}_{-0.06}$	$0.10^{+0.01}_{-0.02}/3.19^{+1.20}_{-1.35}$	$2.59^{+0.07}_{-0.07}/-25.72^{+23.31}_{-71.80}$	c
f090d_brt_cosmos_122	150.1068407	2.227158	24.98	22.59	$5.61^{+0.14}_{-0.14}$	$1.81^{+0.02}_{-0.02}$	$1.51^{+0.19}_{-0.16}$	$-/10.24^{+0.01}_{-0.13}$	$\ldots/0$	$0.6/0.54^{+0.04}_{-0.04}$	$-/3.43^{+0.47}_{-1.00}$	$-/-0.81^{+0.01}_{-0.23}$	d
f090d_brt_cosmos_180	150.0905478	2.2441653	24.27	21.34	$8.36^{+0.21}_{-0.32}$	$1.99^{+0.02}_{-0.02}$	$1.69^{+0.21}_{-0.16}$	$-/10.76^{+0.02}_{-0.01}$	$\ldots/0$	$-/0.46^{+0.05}_{-0.04}$	$-/0.78^{+0.28}_{-0.34}$	$-/-0.26^{+0.14}_{-13.61}$	d
f090d_brt_cosmos_507	150.0991287	2.3206993	25.43	22.52	$8.36^{+0.22}_{-0.49}$	$2.33^{+0.02}_{-0.02}$	$2.07^{+0.18}_{-0.21}$	$-/10.66^{+0.01}_{-0.01}$	$\ldots/0$	$-/0.30^{+0.06}_{-0.05}$	$-/2.43^{+0.56}_{-0.61}$	$-/-18.98^{+18.22}_{-53.49}$	d
f090d_brt_cosmos_611	150.1434149	2.3486737	25.38	23.86	$1.51^{+0.19}_{-0.19}$	$1.41^{+0.07}_{-0.07}$	$1.04^{+0.18}_{-0.19}$	$9.59^{+0.09}_{-0.12}/8.98^{+0.01}_{-0.01}$	$\ldots/0$	$0.1/0.43^{+0.04}_{-0.13}$	$2.02^{+0.75}_{-0.76}/0.32^{+1.97}_{-0.30}$	$-0.61^{+0.27}_{-0.59}/-0.47^{+0.02}_{-0.02}$	c
f090d_brt_cosmos_825	150.1733887	2.4007302	24.87	22.70	$2.93^{+0.23}_{-0.20}$	$3.59^{+0.02}_{-0.02}$	$3.16^{+0.55}_{-0.27}$	$9.97^{+0.14}_{-0.06}/10.64^{+0.01}_{-0.01}$	$\ldots/0$	$0.6/0.35^{+0.05}_{-0.06}$	$0.03^{+0.01}_{-0.01}/1.44^{+0.61}_{-1.27}$	$2.55^{+0.55}_{-0.13}/1.74^{+0.01}_{-0.01}$	irr
f090d_brt_cosmos_882	150.1479556	2.4300038	25.21	22.14	$1.58^{+0.16}_{-0.14}$	$1.87^{+0.01}_{-0.01}$	$1.22^{+0.20}_{-0.15}$	$-/10.16^{+0.01}_{-0.01}$	$\ldots/0$	$0.7/0.62^{+0.04}_{-0.04}$	$-/3.19^{+0.33}_{-0.37}$	$-/-0.58^{+0.01}_{-0.01}$	d
f090d_brt_cosmos_939	150.1830083	2.4695256	24.09	22.50	$1.58^{+0.15}_{-0.14}$	$1.65^{+0.04}_{-0.04}$	$1.23^{+0.19}_{-0.15}$	$-/9.99^{+0.01}_{-0.01}$	$\ldots/0$	$0.4/0.37^{+0.04}_{-0.04}$	$-/3.40^{+0.98}_{-0.51}$	$-/-0.35^{+0.01}_{-0.01}$	d
f115d_brt_cosmos_009	150.1010045	2.1736321	24.29	21.76	$6.39^{+0.15}_{-0.15}$	$2.41^{+0.00}_{-0.00}$	$1.74^{+0.24}_{-0.22}$	$-/10.72^{+0.01}_{-0.01}$	$\ldots/0$	$-/0.82^{+0.12}_{-0.09}$	$-/0.62^{+2.48}_{-0.56}$	$-/-0.86^{+0.03}_{-0.04}$	d
f115d_brt_cosmos_073	150.0969656	2.2288968	24.55	22.32	$7.79^{+0.14}_{-0.14}$	$2.48^{+0.02}_{-0.02}$	$1.98^{+0.19}_{-0.15}$	$-/10.33^{+0.01}_{-0.01}$	$\ldots/0$	$-/0.70^{+0.04}_{-0.04}$	$-/0.77^{+0.36}_{-0.40}$	$-/-1.66^{+0.00}_{-0.00}$	d
f115d_brt_cosmos_142	150.0603007	2.2673313	24.67	22.74	$8.76^{+0.16}_{-0.15}$	$1.97^{+0.02}_{-0.02}$	$1.52^{+0.19}_{-0.17}$	$-/9.95^{+0.01}_{-0.01}$	$\ldots/0$	$-/0.60^{+0.04}_{-0.04}$	$-/0.33^{+2.29}_{-0.31}$	$-/-2.71^{+1.73}_{-4.75}$	d
f115d_brt_cosmos_208	150.057066	2.292873	24.56	21.76	$4.00^{+0.14}_{-0.14}$	$3.13^{+0.03}_{-0.03}$	$1.99^{+0.20}_{-0.15}$	$11.41^{+0.03}_{-0.04}/10.92^{+0.01}_{-0.01}$	$\ldots/0$	$0.4/0.69^{+0.04}_{-0.04}$	$0.37^{+0.03}_{-0.03}/0.83^{+0.28}_{-0.29}$	$-4.16^{+1.66}_{-1.31}/-5.95^{+5.68}_{-16.30}$	irr
f115d_brt_cosmos_338	150.1748959	2.3527429	25.21	23.20	$9.15^{+1.34}_{-0.45}$	$3.08^{+0.03}_{-0.03}$	$2.96^{+0.31}_{-0.22}$	$-/10.39^{+0.09}_{-0.01}$	$\ldots/0$	$-/0.57^{+0.06}_{-0.06}$	$-/0.78^{+0.49}_{-0.52}$	$-/-1.92^{+0.01}_{-0.05}$	irr
f150d_brt_cosmos_119	150.0597858	2.2810155	25.22	23.35	$3.42^{+0.30}_{-1.29}$	$4.23^{+0.08}_{-0.08}$	$2.09^{+0.18}_{-0.21}$	$10.20^{+0.04}_{-0.04}/10.52^{+0.01}_{-0.01}$	$\ldots/0$	$1.0/0.68^{+0.04}_{-0.06}$	$1.49^{+1.09}_{-0.43}/1.79^{+1.71}_{-0.65}$	$3.48^{+0.09}_{-0.08}/-13.08^{+12.30}_{-39.87}$	d
f150d_brt_cosmos_182	150.1915483	2.3146803	26.45	25.17	$2.24^{+0.85}_{-0.19}$	$3.39^{+0.15}_{-0.15}$	$3.01^{+0.44}_{-0.37}$	$9.41^{+0.26}_{-0.29}/9.84^{+0.01}_{-0.01}$	$\ldots/0$	$0.9/0.33^{+0.15}_{-0.09}$	$0.04^{+1.27}_{-0.02}/1.22^{+0.69}_{-0.57}$	$2.68^{+0.97}_{-0.95}/-9.72^{+8.72}_{-26.42}$	c
f150d_brt_cosmos_257	150.1625839	2.3540574	24.95	23.75	$8.74^{+0.17}_{-0.14}$	$2.17^{+0.09}_{-0.09}$	$1.79^{+0.19}_{-0.19}$	$-/9.95^{+0.02}_{-0.01}$	$\ldots/0$	$-/0.60^{+0.04}_{-0.04}$	$-/0.85^{+0.31}_{-0.29}$	$-/-6.50^{+5.42}_{-17.24}$	d
f200d_brt_cosmos_389	150.1006761	2.3348299	25.81	24.93	$4.59^{+0.21}_{-0.40}$	$5.72^{+0.04}_{-0.04}$	$4.95^{+0.42}_{-0.50}$	$10.49^{+0.10}_{-0.65}/10.67^{+0.01}_{-0.01}$	$\ldots/0$	$0.7/0.54^{+0.08}_{-0.08}$	$0.59^{+0.35}_{-0.55}/0.48^{+0.44}_{-0.40}$	$1.79^{+0.84}_{-0.15}/-2.94^{+3.00}_{-8.70}$	d
f090d_brt_jsmed_157	53.0790797	-27.8730445	27.07	25.05	$0.10^{+0.07}_{-0.07}$	$0.89^{+0.01}_{-0.01}$	$0.74^{+0.19}_{-0.16}$	$-/8.30^{+0.01}_{-0.01}$	$\ldots/0$	$-/0.04^{+0.06}_{-0.04}$	$-/5.97^{+0.36}_{-1.48}$	$-/-48.82^{+45.36}_{-140.11}$	d
f090d_brt_jsmed_189	53.0475035	-27.8704957	26.43	22.39	$4.16^{+0.16}_{-0.14}$	$3.72^{+0.01}_{-0.01}$	$3.98^{+0.18}_{-0.14}$	$11.11^{+0.03}_{-0.04}/10.65^{+0.01}_{-0.01}$	$\ldots/0$	$0.2/0.29^{+0.05}_{-0.04}$	$0.49^{+0.05}_{-0.04}/0.22^{+0.29}_{-0.21}$	$-0.43^{+0.26}_{-0.14}/-1.20^{+0.83}_{-2.10}$	irr
f090d_brt_jsmed_386	53.0875763	-27.840385	27.09	23.79	$1.39^{+0.14}_{-0.14}$	$2.02^{+0.00}_{-0.00}$	$1.58^{+0.25}_{-0.23}$	$9.17^{+0.30}_{-0.40}/9.88^{+0.01}_{-0.01}$	$\ldots/0$	$0.8/0.29^{+0.07}_{-0.06}$	$0.39^{+0.34}_{-0.36}/3.11^{+1.52}_{-0.64}$	$1.10^{+1.63}_{-0.46}/-24.57^{+22.91}_{-71.51}$	irr
f090d_brt_uds_014	34.4826496	-5.2862261	25.65	23.00	$1.84^{+0.15}_{-0.18}$	$1.75^{+0.06}_{-0.06}$	$1.23^{+0.24}_{-0.20}$	$10.14^{+0.14}_{-0.16}/9.88^{+0.01}_{-0.03}$	$\ldots/0.35^{+0.31}_{-0.31}$	$0.2/0.37^{+0.10}_{-0.16}$	$1.57^{+1.09}_{-0.51}/1.72^{+3.72}_{-0.94}$	$-0.12^{+0.68}_{-0.68}/-37.08^{+24.23}_{-24.09}$	c
f090d_brt_uds_055	34.4650194	-5.2724489	25.61	25.48	$0.60^{+0.14}_{-0.14}$	$0.95^{+0.01}_{-0.01}$	$1.35^{+0.30}_{-0.32}$	$7.69^{+0.26}_{-0.40}/8.65^{+0.01}_{-0.01}$	$\ldots/0.57^{+0.48}_{-0.46}$	$1.0/0.03^{+0.04}_{-0.03}$	$0.23^{+2.21}_{-0.22}/0.57^{+1.77}_{-0.46}$	$0.87^{+0.28}_{-0.41}/-12.48^{+6.94}_{-6.74}$	c
f090d_brt_uds_107	34.495778	-5.2554256	25.57	22.60	$8.59^{+0.15}_{-0.14}$	$2.37^{+0.07}_{-0.07}$	$1.98^{+0.17}_{-0.17}$	$-/10.55^{+0.01}_{-0.01}$	0	$-/0.54^{+0.06}_{-0.06}$	$-/1.05^{+1.77}_{-0.93}$	$-/-1.23^{+0.01}_{-0.01}$	d
f090d_brt_uds_276	34.3264188	-5.1373572	26.69	23.68	$5.40^{+0.14}_{-0.14}$	$2.91^{+0.01}_{-0.01}$	$5.94^{+0.20}_{-0.17}$	$10.25^{+0.04}_{-0.04}/10.64^{+0.01}_{-0.01}$	$\ldots/0$	$0.6/0.12^{+0.04}_{-0.04}$	$0.11^{+0.02}_{-0.02}/0.22^{+0.27}_{-0.27}$	$3.37^{+0.09}_{-0.08}/-0.88^{+0.83}_{-2.07}$	irr
f090d_brt_uds_292	34.3199395	-5.1346201	24.93	21.81	$1.68^{+0.16}_{-0.17}$	$2.14^{+0.00}_{-0.00}$	$1.16^{+0.23}_{-0.21}$	$-/10.26^{+0.01}_{-0.01}$	$\ldots/0.07^{+0.15}_{-0.07}$	$-/0.78^{+0.08}_{-0.08}$	$-/0.76^{+2.12}_{-0.59}$	$-/-14.28^{+11.60}_{-11.87}$	c
f090d_brt_uds_322	34.419778	-5.1265324	24.54	22.90	$1.60^{+0.14}_{-0.14}$	$1.47^{+0.03}_{-0.03}$	$1.43^{+0.24}_{-0.24}$	$10.90^{+0.05}_{-0.17}/10.03^{+0.01}_{-0.01}$	$\ldots/0.41^{+0.36}_{-0.36}$	$0.0/0.04^{+0.05}_{-0.05}$	$3.56^{+0.74}_{-6.73}/3.09^{+0.88}_{-0.97}$	$2.94^{+0.22}_{-6.73}/-66.47^{+43.24}_{-43.08}$	c
f090d_brt_uds_324	34.3416163	-5.1254591	24.27	21.88	$1.59^{+0.14}_{-0.14}$	$1.72^{+0.00}_{-0.00}$	$1.05^{+0.18}_{-0.19}$	$10.87^{+0.07}_{-0.12}/10.07^{+0.01}_{-0.01}$	$\ldots/0$	$0.2/0.55^{+0.07}_{-0.06}$	$-/0.82^{+0.59}_{-0.41}$	$-/-5.92^{+5.05}_{-16.68}$	d
f115d_brt_uds_161	34.3434954	-5.2761198	24.48	22.91	$1.60^{+0.14}_{-0.14}$	$2.47^{+0.02}_{-0.02}$	$2.34^{+0.23}_{-0.26}$	$10.26^{+0.08}_{-0.06}/10.49^{+0.01}_{-0.02}$	$\ldots/0$	$0.5/0.08^{+0.06}_{-0.06}$	$0.68^{+0.17}_{-0.14}/2.25^{+0.51}_{-0.69}$	$2.04^{+1.30}_{-0.73}/-17.47^{+16.51}_{-50.14}$	irr
f115d_brt_uds_193	34.403946	-5.268707	26.72	23.95	$2.07^{+0.18}_{-0.17}$	$3.09^{+0.09}_{-0.09}$	$2.86^{+0.39}_{-0.38}$	$11.27^{+0.05}_{-0.32}/10.39^{+0.01}_{-0.03}$	$\ldots/0.08^{+0.16}_{-0.08}$	$1.0/0.28^{+0.12}_{-0.12}$	$0.02^{+1.01}_{-0.01}/1.68^{+0.58}_{-0.66}$	$2.14^{+0.48}_{-0.77}/-35.50^{+23.48}_{-24.46}$	c
f115d_brt_uds_221	34.34927	-5.2634548	24.11	21.73	$6.94^{+0.17}_{-0.14}$	$2.40^{+0.08}_{-0.08}$	$1.70^{+0.28}_{-0.27}$	$-/10.74^{+0.01}_{-0.02}$	$\ldots/0.15^{+0.19}_{-0.15}$	$-/0.68^{+0.08}_{-0.08}$	$-/0.79^{+0.74}_{-0.54}$	$-/-5.25^{+5.55}_{-18.69}$	irr
f115d_brt_uds_263	34.2904198	-5.2531251	27.05	24.88	$2.06^{+0.41}_{-0.23}$	$3.03^{+0.11}_{-0.11}$	$2.29^{+0.45}_{-0.34}$	$9.69^{+0.72}_{-0.57}/9.86^{+0.01}_{-0.02}$	$\ldots/0$	$0.9/0.36^{+0.07}_{-0.07}$	$0.03^{+0.08}_{-0.01}/1.91^{+0.92}_{-0.94}$	$1.34^{+0.26}_{-0.32}/-15.17^{+13.78}_{-42.63}$	c
f115d_brt_uds_606	34.4056603	-5.1556666	24.80	23.25	$2.20^{+0.14}_{-0.14}$	$2.46^{+0.00}_{-0.00}$	$2.14^{+0.29}_{-0.24}$	$9.57^{+0.24}_{-0.21}/10.31^{+0.01}_{-0.01}$	$\ldots/0.20^{+0.28}_{-0.20}$	$0.2/0.11^{+0.07}_{-0.07}$	$3.16^{+0.26}_{-0.21}/2.56^{+0.60}_{-0.50}$	$-3.45^{+7.38}_{-1.91}/-55.14^{+37.26}_{-35.41}$	c
f115d_brt_uds_620	34.3343455	-5.1520742	24.89	23.47	$2.40^{+0.14}_{-0.14}$	$2.57^{+0.00}_{-0.00}$	$2.28^{+0.22}_{-0.21}$	$11.00^{+0.03}_{-0.03}/10.18^{+0.01}_{-0.02}$	$\ldots/0$	$0.4/0.36^{+0.05}_{-0.05}$	$0.62^{+0.06}_{-0.05}/0.74^{+0.40}_{-0.50}$	$-3.09^{+6.92}_{-0.59}/-5.41^{+4.67}_{-14.32}$	d
f115d_brt_uds_666	34.3843112	-5.140298	26.63	23.80	$8.68^{+0.18}_{-0.16}$	$2.92^{+0.03}_{-0.03}$	$2.20^{+0.34}_{-0.29}$	$-/10.25^{+0.01}_{-0.01}$	$\ldots/0.24^{+0.23}_{-0.23}$	$-/0.68^{+0.12}_{-0.17}$	$-/1.09^{+1.24}_{-0.72}$	$-/-22.90^{+15.31}_{-15.19}$	c
f115d_brt_uds_667	34.2848298	-5.1407918	24.49	22.03	$2.13^{+0.17}_{-0.16}$	$2.22^{+0.20}_{-0.20}$	$1.98^{+0.23}_{-0.17}$	$9.34^{+0.58}_{-0.31}/10.89^{+0.01}_{-0.03}$	$\ldots/0.12^{+0.17}_{-0.12}$	$0.4/0.41^{+0.06}_{-0.10}$	$1.65^{+0.92}_{-0.37}/2.47^{+0.71}_{-0.76}$	$0.71^{+0.38}_{-0.10}/-53.15^{+35.53}_{-33.41}$	c
f115d_brt_uds_755	34.2664134	-5.1089223	24.31	22.98	$2.14^{+0.34}_{-0.26}$	$2.49^{+0.01}_{-0.01}$	$2.44^{+0.23}_{-0.19}$	$11.11^{+0.03}_{-0.03}/10.45^{+0.01}_{-0.02}$	$\ldots/0.47^{+0.35}_{-0.35}$	$0.4/0.03^{+0.04}_{-0.03}$	$0.28^{+0.05}_{-0.05}/2.06^{+0.56}_{-0.61}$	$0.38^{+0.56}_{-0.40}/-43.72^{+28.93}_{-29.02}$	c
f150d_brt_uds_063	34.3321593	-5.2880617	25.34	23.67	$11.18^{+0.34}_{-0.30}$	$3.43^{+0.03}_{-0.03}$	$3.62^{+0.52}_{-0.38}$	$-/10.57^{+0.01}_{-0.01}$	$\ldots/0$	$-/0.46^{+0.07}_{-0.06}$	$-/0.35^{+0.38}_{-0.24}$	$-/-0.28^{+1.11}_{-3.25}$	d
f150d_brt_uds_088	34.2522909	-5.275846	26.50	25.50	$2.08^{+0.52}_{-0.27}$	$2.81^{+0.19}_{-0.19}$	$2.85^{+0.54}_{-0.69}$	$9.57^{+0.24}_{-0.21}/9.60^{+0.01}_{-0.04}$	$\ldots/0.31^{+0.31}_{-0.31}$	$1.0/0.11^{+0.17}_{-0.09}$	$1.34^{+0.89}_{-1.33}/1.60^{+0.71}_{-0.75}$	$1.34^{+0.75}_{-1.31}/-34.16^{+21.89}_{-21.63}$	c
f150d_brt_uds_158	34.3031646	-5.2504972	26.37	25.49	$3.39^{+7.41}_{-0.41}$	$3.44^{+0.16}_{-0.16}$	$2.17^{+0.87}_{-0.52}$	$11.00^{+0.03}_{-0.03}/9.45^{+0.07}_{-0.07}$	$\ldots/0$	$0.4/0.29^{+0.13}_{-0.15}$	$0.03^{+0.11}_{-0.01}/1.52^{+1.45}_{-0.94}$	$2.62^{+0.75}_{-0.97}/-11.41^{+9.87}_{-32.89}$	c
f150d_brt_uds_159	34.4929619	-5.2500532	25.57	24.26	$2.80^{+0.14}_{-0.14}$	$3.53^{+0.03}_{-0.03}$	$2.82^{+0.33}_{-0.33}$	$9.34^{+0.58}_{-0.31}/10.26^{+0.01}_{-0.05}$	$\ldots/0.03^{+0.10}_{-0.03}$	$0.7/0.42^{+0.10}_{-0.10}$	$0.03^{+0.08}_{-0.01}/0.92^{+0.68}_{-0.68}$	$2.57^{+1.17}_{-0.77}/-10.62^{+10.00}_{-18.68}$	c
f150d_brt_uds_333	34.2934613	-5.1547235	24.73	23.02	$8.80^{+0.14}_{-0.14}$	$2.62^{+0.03}_{-0.03}$	$2.06^{+0.21}_{-0.23}$	$-/10.38^{+0.01}_{-0.01}$	$\ldots/0$	$-/0.83^{+0.08}_{-0.07}$	$-/1.43^{+1.43}_{-1.09}$	$-/-1.21^{+0.01}_{-0.01}$	c
f200d_brt_uds_133	34.2840954	-5.2605105	25.23	24.52	$2.79^{+0.14}_{-0.14}$	$5.06^{+0.08}_{-0.08}$	$2.86^{+0.22}_{-0.26}$	$9.69^{+0.72}_{-0.57}/10.43^{+0.01}_{-0.01}$	$\ldots/0$	$0.9/0.58^{+0.09}_{-0.09}$	$0.05^{+0.05}_{-0.02}/1.92^{+0.36}_{-0.48}$	$1.94^{+0.15}_{-0.23}/-14.39^{+13.66}_{-42.56}$	d
f200d_brt_uds_154	34.2734842	-5.2513303	26.23	25.36	$2.61^{+0.22}_{-0.20}$	$5.86^{+0.17}_{-0.17}$	$2.62^{+0.54}_{-0.52}$	$9.57^{+0.24}_{-0.21}/10.03^{+0.01}_{-0.05}$	$\ldots/0$	$0.9/0.77^{+0.16}_{-0.18}$	$0.16^{+1.72}_{-0.13}/1.54^{+0.98}_{-0.86}$	$1.33^{+0.95}_{-0.63}/0.48^{+0.31}_{-24.93}$	c

Note. Similar to Table 6 but for the Tier 2 objects in the "low-z" category.

Figure 4. Left: F356W magnitude distributions for all objects, and objects in the "high-z," "low-z," and "undecided" categories, respectively. Right: Contour plots of Age vs. $E(B - V)$ for the objects in the "high-z" (blue) and "low-z" (red) categories. Both parameters are the 50th percentile values from the CIGALE run (using those from the Le Phare run gives similar results). The overlaid data points represent the SED fitting results of the seven spectroscopically confirmed grade I objects in Table 8 (see Section 6) when fixing the redshifts to their z_{spec}; the only confirmed high-z object is shown in blue, while all other objects (all at low redshifts) are shown in gold.

can be classified as EROs under the fiducial criterion of $m_{115} - m_{356} > 2.0$ mag. In total, 80%, 87%, and 63% of the objects in the "high-z," "low-z," and "undecided" categories can be classified as EROs, respectively.

Figure 4 shows the distribution of the fitted age and $E(B - V)$ for the "low-z" and "high-z" objects, which are the two most important (and degenerated) parameters that might give low-z galaxies red colors mimicking those of high-z galaxies. As evident in the figure, the regions occupied by the two categories are not well separated. The contours of the "high-z" objects make a thin slab at the age of $\sim$0.25 Gyr, which is largely due to the constraint that the age of a galaxy cannot be older than that of the universe at the fitted high redshift. However, the region of the "low-z" objects also extends to very close to this area.

Using the SED fitting results by CIGALE, we also examined the fraction of stellar mass formed in the recent burst for each object in the "high-z" and "low-z" categories. We found that there are significant differences: the "high-z" candidates tend to have large burst fractions (median $\sim$55%), suggesting that a considerable portion of their stellar mass had been formed in a recent burst. In contrast, the "low-z" candidates exhibit little burst activity (median near zero). Considering the generally young ages of the "high-z" candidates, these results further suggests that they are dominated by young and bursty star-forming populations, whereas the "low-z" objects are characterized by older stellar populations with nonbursty star formation histories.

Another interesting point revealed in our SED analysis is that incorporating mid-IR photometry, while being helpful, still does not provide a decisive factor to separate the low-z and high-z candidates. For example, contrary to what one might naively believe, being bright in mid-IR does not necessarily preclude a good SED fit to give a high-z solution (see Figure 3).

6. Spectroscopic Identifications

As it turns out, 10 of our bright dropouts in the main sample have existing NIRSpec spectroscopic data, which we used to identify their redshifts. These data are from the following programs: PID 1213 (PI N. Luetzgendorf), 1215 (PI N. Luetzgendorf), 4233 (PIs A. de Graaff & G. Brammer), and 6585 (PI D. Coulter). We used the data taken in the PRISM

mode, which cover the range of 0.6–5.3 μm with the resolving power of $R \approx 30$–300.

We reduced these data on our own. We first retrieved the Level 1b products from MAST and processed them through the `calwebb_detector1` step of the JWST pipeline (version 1.14.0) in the context of `jwst_1234.pmap`. The output "rate. fits" files were then processed through the MSAEXP package (G. Brammer 2023, version 0.8.4), which provides an end-to-end reduction including the final extraction of spectra. Briefly, the procedure removes the so-called "$1/f$" noise pattern, detects and masks the "snowball" defects, subtracts the bias level, applies the flat-field, corrects the path-loss, does the flux calibration, traces spectra on all single exposures, and combines the single exposures with outlier rejection. All data used in this work were taken under the three-shutter setup. In most cases, the background was subtracted using the measurements in the nearest blank slit before drizzling individual exposures onto a common pixel grid. A few of our sources extend to all shutters, and the background could not be estimated locally. In such cases, the background was estimated using a nearby slit that was relatively blank.

Among the 10 objects, seven have highly reliable redshifts based on at least two emission lines, which we rank as grade "I." Two have only a single line, which we assume to be Hα due to a marginal detection that could be [O III] that yields a consistent redshift. These two identifications are ranked as grade "II." One other does not show any emission lines and cannot be identified, which we assign grade "III." The results are summarized in Table 8.

While still limited, these spectroscopic identifications are broadly consistent with our SED analysis that most of the bright dropouts should be at low redshifts. In terms of the accuracy of our categorization, the picture is mixed. Among the seven with grade I z_{spec}, two are the candidates in our "low-z" category, three are in the "high-z" category, and two are in the "undecided" category. The two "low-z" ones are indeed confirmed to be at $z \approx 3$. One of the three "high-z" candidates, which is a T2 F115W dropout with a compact morphology, is confirmed at $z_{spec} = 8.679$ (this is a recovery of the identification by A. Zitrin et al. 2015 made in the pre-JWST era, which will be further discussed in Section 7). However, two other "high-z" candidates (one T1 F150W dropout and one T2

Table 8
NIRSpec/MSA Identifications of Very Bright Dropouts

SID	Category (Tier)/Morph	$z_{\rm spec}$	$z_{\rm lp}$	$z_{\rm ez}$	$z_{\rm cg}$	T (Myr)	$E(B-V)$	$\log_{10}(M_*/M_\odot)$
f115d_brt_uds_245	High-z (T2)/irr	2.53 (I)	$8.78^{+0.15}_{-0.14}$	$2.46^{+0.02}_{-0.02}$	$8.55^{+1.47}_{-1.47}$	$-/576 \pm 328$	$-/0.44 \pm 0.07$	$-/10.61 \pm 0.06$
f115d_brt_cosmos_344	Undecided/irr	2.99 (I)	$8.49^{+0.24}_{-0.49}$	$3.10^{+0.03}_{-0.03}$	$3.38^{+1.26}_{-1.26}$	$-/1015 \pm 592$	$-/0.56 \pm 0.10$	$-/10.69 \pm 0.14$
f150d_brt_ceers_113	Undecided/c	3.10 (I)	$15.38^{+0.15}_{-0.14}$	$3.98^{+0.01}_{-0.01}$	$3.09^{+2.18}_{-2.18}$	$-/934 \pm 288$	$-/0.40 \pm 0.07$	$-/10.40 \pm 0.05$
f115d_brt_ceers_279	Low-z (T2)/c	3.21 (I)	$1.14^{+0.17}_{-0.14}$	$2.64^{+0.06}_{-0.06}$	$1.01^{+0.22}_{-0.22}$	$1575^{+217}_{-524}/1010 \pm 87$	$0.0/0.00 \pm 0.01$	$10.08^{+0.05}_{-0.25}/9.99 \pm 0.02$
f115d_brt_uds_685	Low-z (T1)/e	3.23 (I)	$3.17^{+0.17}_{-0.16}$	$3.41^{+0.06}_{-0.06}$	$2.74^{+0.24}_{-0.24}$	$229^{+710}_{-206}/913 \pm 718$	$1.0/0.57 \pm 0.11$	$10.25^{+0.44}_{-0.25}/10.77 \pm 0.11$
f150d_brt_ceers_051	High-z (T1)/c	3.46 (I)	$12.22^{+0.24}_{-0.28}$	$14.57^{+0.01}_{-0.01}$	$14.37^{+0.80}_{-0.80}$	$34^{+71}_{-19}/665 \pm 360$	$0.8/0.68 \pm 0.10$	$9.84^{+0.18}_{-0.22}/10.38 \pm 0.10$
f115d_brt_ceers_062	High-z (T2)/c	8.679 (I)	$8.80^{+0.14}_{-0.14}$	$8.88^{+0.01}_{-0.01}$	$8.95^{+0.12}_{-0.12}$	$-/13 \pm 8$	$-/0.15 \pm 0.04$	$-/9.10 \pm 0.08$
f150d_brt_uds_158	Low-z (T2)/c	3.72 (II)	$3.39^{+7.41}_{-0.41}$	$3.44^{+0.16}_{-0.16}$	$2.45^{+0.90}_{-0.90}$	$82^{+454}_{-63}/1073 \pm 365$	$0.4/0.08 \pm 0.10$	$9.22^{+0.38}_{-0.25}/9.75 \pm 0.07$
f200d_brt_uds_154	Low-z (T2)/c	4.56 (II)	$2.61^{+0.22}_{-0.20}$	$5.86^{+0.17}_{-0.17}$	$2.83^{+1.13}_{-1.13}$	$32^{+56}_{-18}/915 \pm 136$	$1.0/0.40 \pm 0.07$	$9.23^{+0.56}_{-0.37}/10.37 \pm 0.09$
f115d_brt_ceers_146	Low-z (T1)/d	N/A (III)	$1.80^{+0.15}_{-0.15}$	$2.64^{+0.06}_{-0.06}$	$1.75^{+0.33}_{-0.33}$	$\cdots$	$\cdots$	$\cdots$

Note. The Roman numerals in parenthesis in the $z_{\rm spec}$ column indicate the reliability of the spectroscopic redshifts: I—$z_{\rm spec}$ determined using $\geqslant 2$ high S/N emission lines; II—only one high S/N emission line is present, and $z_{\rm spec}$ is determined by assigning the most probable line considering its $z_{\rm phot}$; III—no emission line, i.e., no solid redshift can be determined.
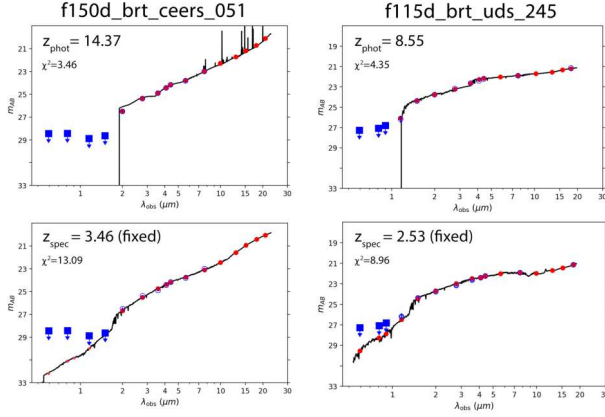
Figure 5. Comparison of SED fittings (using CIGALE for demonstration) for the two "high-z" candidates that were later confirmed as low redshift ones. In both cases, the prominent Balmer break at low-z mimics the high-z Lyman-break signature very well. Nonetheless, the high-z solutions provide significantly better fits (as indicated by χ^2), which demonstrates the difficulty in SED fitting.

F115W dropout) turn out to be at low redshifts. The two "undecided" objects are at low redshifts as well. In other words, our "low-z" category seems to be robust, but the "high-z" category is severely contaminated. There are three T1 and seven T2 "high-z" objects in our main sample, and one in each tier has been refuted. Nonetheless, the one that is confirmed at $z_{\rm spec} = 8.679$ shows that there indeed could be bona fide high-z objects in our "high-z" category.

7. Discussion

7.1. Mixture of EROs and High-z Objects

Our SED analysis (see Section 5) shows that the bright dropouts through the NIRCam bands should be dominated by red galaxies at low redshifts, and the limited spectroscopic identifications (see Section 6) are consistent with this interpretation. On the other hand, the SED analysis also shows that these bright dropouts could contain a non-negligible fraction of real high-z objects, which is also confirmed by the spectroscopic identifications. The caveat is that the SED screening for categorization is not ideal for these bright objects: our "high-z" category is severely contaminated, and there is still a large fraction of objects that have to be placed in the "undecided" category. We believe that this is just a manifestation of the limitation of SED fitting as a method in general: some low-z galaxies can indeed have SEDs very similar to those of high-z galaxies, even when the photometry is extended to mid-IR. To further demonstrate this limitation reflected in the two refuted "high-z" candidates, we ran CIGALE SED fitting using the same configuration as in Section 5.1 but with the redshift fixed at their $z_{\rm spec}$. Figure 5 compares their best-fit SED models when redshift is freed and fixed. Obviously, it is the strong Balmer break effectively mimicking the Lyman-break signature that leads to the high-z solution, which is a situation often encountered when the veto bands are not deep enough. In fact, the high-z solution gives a better fit in both cases, as judged by the χ^2 values. This is also seen in the two refuted sources in J. A. Zavala et al. (2023) and P. Arrabal Haro et al. (2023a): both appear in our supplement sample as f200d_brt_ceers_264 and f150d_brt_ceers_191. Although they lie outside the MIRI footprint, their dropout signature is also caused by the strong Balmer break.

In short, it is difficult for any SED fitting tools/templates to break the degeneracy when lacking very deep veto band images. On the other hand, the high fraction of low-z interlopers at the very bright end suggests that apparent brightness itself could be used as a prior to prescreen the dropouts to retain a relatively pure high-z sample, e.g., using $m_{356} \gtrsim 25$–26 mag ($M_{\rm UV} \gtrsim -22$ mag), which has already been adopted in several selections (e.g., R. J. Bouwens et al. 2023; H. Yan et al. 2023b; N. J. Adams et al. 2024, etc.).

7.2. Implication of Bright Dropouts at High-z

Bearing the aforementioned caveat in mind, we briefly discuss the implications of the possibility that some of these very bright dropouts could indeed be at high-z. If they are at $z > 6$, as their $z_{\rm phot}$ indicates they must be the most extraordinary galaxies in the early universe. The recovered high-z object, f115d_brt_ceers_062 at $z = 8.679$ (see also P. Arrabal Haro et al. 2023b; Y. Isobe et al. 2023; R. L. Larson et al. 2023b; M. Tang et al. 2023, for the previous JWST identifications of the same object), is a good example. Interestingly, it has $m_{115} - m_{356} = 1.52$ mag, which does not meet the ERO criterion that we adopt here but is very close. This galaxy was noted for its unusual brightness at such a high redshift and even more so for its very red color between the HST WFC3 F160W band ($\sim 1.6\,\mu m$) and the Spitzer IRAC Channel 2 ($\sim 4.5\,\mu m$), the latter of which was attributed to the strong [O III] emission lines being shifted to $\sim 4.8\,\mu m$ (A. Zitrin et al. 2015). The JWST spectrum confirms that it is indeed the case. This indicates that the galaxy has very active ongoing star formation, which is the reason that it is so luminous in the rest-frame UV ($M(1500\,\text{Å}) = -22.4$ mag). As shown in Figure 6, the SED fitting by CIGALE at its $z_{\rm spec}$ gives the instantaneous SFR $= 232.9 \pm 80.5 M_{\odot}\,{\rm yr}^{-1}$, which makes it qualified as a starburst. This extremely high SFR is the result of its high stellar mass ($M_* = 10^{9.1} M_{\odot}$) and very young age ($T = 12.7 \pm 7.8$ Myr), the latter of which is needed to explain its very blue UV emission. In fact, even with such an extreme solution, its $m_{150} - m_{200}$ color is still not well explained; it is likely that an IMF more top-heavy than currently adopted will be necessary (e.g., C. A. Mason et al. 2023).

Recent theoretical models could explain the number density of high-z UV-luminous galaxies to some extent (see e.g., A. Dekel et al. 2023; A. Ferrara et al. 2023; X. Shen et al. 2023). However, it is still challenging for these new models to produce a number density at $M_{\rm UV} \lesssim -23$ mag that could lead to positive detections within the volume that has been surveyed by the JWST. Our "high-z" categories contain a significant number of objects at $M_{\rm UV} < -23.5$ mag, if they are indeed at high redshifts. Of course, their high luminosities could be explained if they host AGNs (see e.g., I. Labbé et al. 2023); however, one would then need to explain the existence of supermassive black holes in such early times.

Therefore, we argue that these extreme objects should not be simply ignored. On the contrary, spectroscopic identification of them (confirmation or rejection) will provide a valuable test of the early galaxy formation theories. If confirmed, the most challenging aspect will be explaining their stellar masses. Given their brightnesses in the two reddest NIRCam bands (F356W and F444W), not only starburst-like SFRs but also very high stellar masses will be required to fit their SEDs reasonably. Some of our objects will have to have $M_* \sim 10^{11} M_{\odot}$, which, to our knowledge, cannot be produced in any new models of the early Universe.
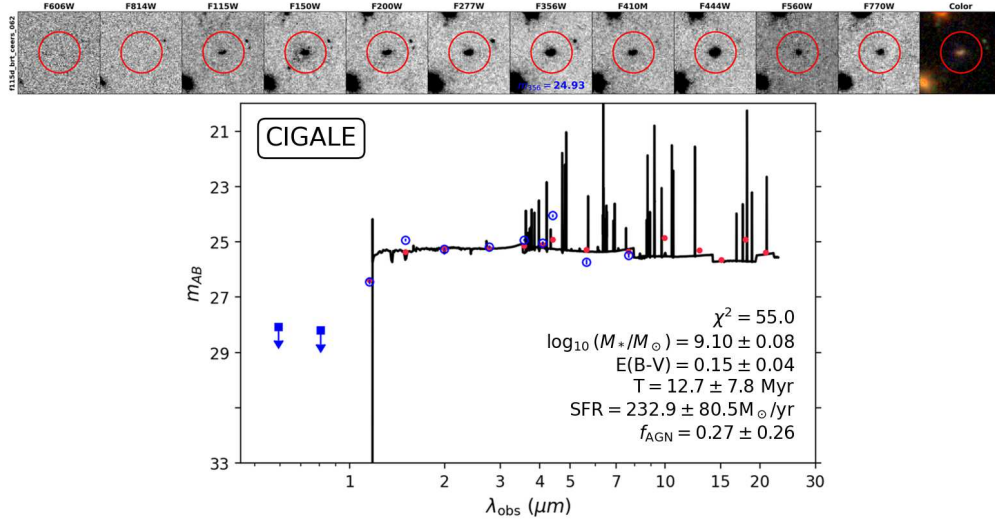
Figure 6. Image stamps of `f115d_brt_ceers_062` (top) and its SED fitting results from CIGALE (bottom). This is a known galaxy at $z_{\rm spec} = 8.679$ recovered in our selection. The image stamps are similar to those shown in Figure 1. The SED fitting plot is similar to those shown in Figure 3, but is obtained by running CIGALE at the fixed $z = 8.679$. The most important output physical parameters are shown.

8. Summary

We present a systematic study of very bright dropouts in the successive JWST NIRCam passbands, which was carried out using public data in four blank fields over $500\,{\rm arcmin}^2$. These objects were selected following the classic dropout method that is widely used to search for Lyman-break galaxies at high redshifts, with the only additional requirement that they must be very bright: the F090W and F115W dropouts must have $m_{356} \leqslant 25.1\,{\rm mag}$, and the F150W and F200W dropouts must have $m_{356} \leqslant 26.0\,{\rm mag}$. In total, 300 very bright dropouts were selected. We then focused on the 137 objects that fall within the coverage of the MIRI observations ($\sim 200\,{\rm arcmin}^2$ of overlapping area), which form the main sample of this work. The rationale was that the inclusion of the mid-IR measurements would constrain the SEDs more stringently. Using the fiducial criterion of $m_{115} - m_{356} > 2.0\,{\rm mag}$ for the ERO selection, the vast majority of them (81%) would qualify as EROs, although the usual ERO selection does not impose the criterion of nondetections in the veto bands as the dropout selection does. The goal of this study is to understand the nature of such very bright dropouts; in particular, how they overlap with the ERO population at low redshifts and whether any of them could be high-z LBGs as the dropout method means to select.

For this purpose, we used three different fitting tools to analyze their SEDs independently, each using a different set of fitting templates: Le Phare with the BC03 population synthesis models, EAZY with the spectra of 129 nearby galaxies from M. J. I. Brown et al. (2014) that have mid-IR measurements, and CIGALE with the BC03 models for stars plus the contributions from the nebular gas and the possible AGN component. Based on the derived $z_{\rm phot}$ values, we divided our objects into two categories, the "high-z" category containing objects with $z_{\rm phot} \geqslant 6.0$ and the "low-z" category containing those with $z_{\rm phot} < 6.0$. In each category, we further sorted the objects into Tier 1 and Tier 2 based on the goodness of fits and the internal consistency from three SED fitting tools. Any objects that could not be classified as "high-z" or "low-z" were put in the "undecided" category. In the end, there are 10 objects in "high-z" (80% qualify as EROs), 93 in "low-z" (87% EROs),

and 34 in "undecided" (63% EROs). Therefore, our main conclusions are that (1) the NIRCam-selected very bright dropouts are predominantly ($>67.9\%$) low-z galaxies and (2) a non-negligible fraction ($>7\%$) of them could still be at high-z.

Ten of our objects have existing JWST NIRSpec spectroscopic observations, and we have obtained secure redshifts for seven of them. Among these seven objects, six are at $z \approx 3$ (including two objects in our "high-z" category), and one is the recovery of a known galaxy at $z = 8.679$ that is a Tier 2 object in our "high-z" category. These identifications, while still very limited, are consistent with our conclusions above. Although the "high-z" category is severely contaminated at such a bright level despite the inclusion of the mid-IR data, it does contain at least one genuine high-z object. Most objects in the "high-z" category are brighter than this one, and if more of them are confirmed to be at high-z, they would be in a very high luminosity regime still largely unexplored by the current theoretical models, and explaining their number density and extreme properties (e.g., very high stellar masses and SFRs) could pose a challenge.

Appendix A
The Supplement Sample of Very Bright Dropouts

Among the 300 very bright dropouts, 163 of them are outside of the MIRI coverage, which we did not perform SED analysis due to the lack of the mid-IR data. These objects form our supplement sample, which are listed in Table A1 below.

Table A1
Objects that Do Not have MIRI Coverage

SID	R.A.	Decl.	m_{356}	SID	R.A.	Decl.	m_{356}	SID	R.A.	Decl.	m_{356}
f115d_brt_ceers_021	215.0885078	52.918795	23.80	f115d_brt_ceers_022	214.9938146	52.8521078	23.48	f115d_brt_ceers_031	215.0617498	52.9009611	21.76
f115d_brt_ceers_050	214.9806545	52.848635	22.84	f115d_brt_ceers_056	214.8544341	52.7595908	22.82	f115d_brt_ceers_059	215.0804619	52.9215632	24.15
f115d_brt_ceers_072	214.9396063	52.8255474	24.90	f115d_brt_ceers_074	215.0731942	52.9214419	24.04	f115d_brt_ceers_096	214.8097457	52.7397	23.39
f115d_brt_ceers_098	214.9438718	52.8358337	24.70	f115d_brt_ceers_148	214.9047696	52.8172013	22.62	f115d_brt_ceers_186	214.8607121	52.7968492	22.97
f115d_brt_ceers_189	214.8125544	52.7627987	24.52	f115d_brt_ceers_196	214.8852216	52.8157635	22.98	f115d_brt_ceers_277	214.8098893	52.7894358	24.05
f115d_brt_ceers_305	214.886832	52.8553988	24.96	f115d_brt_ceers_322	214.8099731	52.8097647	23.03	f115d_brt_ceers_327	214.9476307	52.911126	24.63
f115d_brt_ceers_328	214.876975	52.8604127	22.76	f115d_brt_ceers_360	214.7999771	52.8221046	24.08	f115d_brt_ceers_367	215.0368278	52.9935023	23.76
f115d_brt_ceers_371	214.9774813	52.9534984	23.16	f115d_brt_ceers_374	214.8505946	52.8660419	22.99	f115d_brt_ceers_392	214.7914996	52.8380477	22.07
f115d_brt_ceers_397	214.8357213	52.8753275	22.95	f115d_brt_ceers_408	214.8807006	52.9129751	23.27	f115d_brt_ceers_414	214.9040497	52.9327088	22.72
f115d_brt_ceers_422	214.8145038	52.8701449	24.80	f115d_brt_ceers_424	214.8381827	52.8888725	22.91	f115d_brt_ceers_453	214.8521098	52.9097693	22.87
f115d_brt_ceers_456	214.7634114	52.8478132	23.42	f150d_brt_ceers_036	214.8906508	52.8030673	24.57	f150d_brt_ceers_039	214.8829258	52.798169	24.32
f150d_brt_ceers_104	214.723005	52.7397616	24.28	f150d_brt_ceers_118	214.7180938	52.7480989	24.40	f150d_brt_ceers_148	214.9440605	52.9297443	26.15
f150d_brt_ceers_191	214.9145578	52.9430309	26.78	f150d_brt_ceers_201	214.9161447	52.9519038	24.85	f150d_brt_ceers_046	215.0505106	52.9260662	24.44
f200d_brt_ceers_222	214.9315925	52.9210116	24.80	f200d_brt_ceers_264	214.9091331	52.9372118	25.93	f090d_brt_cosmos_014	150.1440391	2.1772542	24.67
f090d_brt_cosmos_018	150.1138723	2.1819308	21.84	f090d_brt_cosmos_044	150.1449324	2.1912166	25.05	f090d_brt_cosmos_058	150.1431031	2.2004338	21.45
f090d_brt_cosmos_090	150.1217583	2.2130011	24.80	f090d_brt_cosmos_100	150.1244376	2.2172783	24.98	f090d_brt_cosmos_109	150.1236108	2.220721	23.89
f090d_brt_cosmos_137	150.1458027	2.2336448	23.46	f090d_brt_cosmos_143	150.1430039	2.2348342	23.69	f090d_brt_cosmos_198	150.1300109	2.2526974	21.99
f090d_brt_cosmos_199	150.1880081	2.2533098	23.56	f090d_brt_cosmos_209	150.1802681	2.2559495	23.51	f090d_brt_cosmos_252	150.1257594	2.2665978	24.13
f090d_brt_cosmos_284	150.089659	2.2758037	22.15	f090d_brt_cosmos_329	150.1393874	2.2822976	23.13	f090d_brt_cosmos_338	150.1859316	2.2831453	21.29
f090d_brt_cosmos_361	150.1816122	2.2895056	23.48	f090d_brt_cosmos_392	150.1394278	2.296584	23.96	f090d_brt_cosmos_421	150.1477821	2.3007552	22.50
f090d_brt_cosmos_454	150.1706349	2.307604	21.96	f090d_brt_cosmos_457	150.0759893	2.3096663	24.27	f090d_brt_cosmos_476	150.1121534	2.3140194	21.37
f090d_brt_cosmos_477	150.1132457	2.3149776	24.47	f090d_brt_cosmos_479	150.1307254	2.3141032	21.68	f090d_brt_cosmos_485	150.1292412	2.3163196	22.16
f090d_brt_cosmos_593	150.0990328	2.3436285	24.96	f090d_brt_cosmos_628	150.078639	2.3523408	24.40	f090d_brt_cosmos_633	150.0776435	2.3530061	24.58
f090d_brt_cosmos_690	150.0712848	2.3605719	23.72	f090d_brt_cosmos_710	150.072502	2.363681	24.74	f090d_brt_cosmos_721	150.0985811	2.3653675	21.09
f090d_brt_cosmos_737	150.1293022	2.3695651	21.33	f090d_brt_cosmos_749	150.1102552	2.3741219	21.57	f090d_brt_cosmos_753	150.0696261	2.3750253	23.42
f090d_brt_cosmos_767	150.085375	2.3801667	22.78	f090d_brt_cosmos_772	150.0698461	2.3815248	22.68	f090d_brt_cosmos_843	150.0823792	2.4033897	21.42
f090d_brt_cosmos_873	150.0952557	2.4233551	22.49	f090d_brt_cosmos_909	150.1307867	2.4443966	24.52	f090d_brt_cosmos_937	150.1269678	2.4653668	21.32
f115d_brt_cosmos_025	150.1197606	2.1886	23.63	f115d_brt_cosmos_107	150.1536777	2.2477695	23.00	f115d_brt_cosmos_119	150.1092878	2.252688	23.39
f115d_brt_cosmos_162	150.1129588	2.2745327	23.79	f115d_brt_cosmos_335	150.096574	2.3520867	24.90	f115d_brt_cosmos_425	150.0864335	2.3953681	24.28
f150d_brt_cosmos_004	150.1289676	2.1741546	24.40	f150d_brt_cosmos_088	150.1365424	2.2605942	23.29	f150d_brt_cosmos_094	150.1510636	2.2623562	22.43
f150d_brt_cosmos_320	150.0935145	2.3947138	24.44	f150d_brt_cosmos_330	150.0925514	2.3981518	24.25	f150d_brt_cosmos_338	150.11263	2.4066739	23.88
f150d_brt_cosmos_352	150.1206107	2.4180919	23.77	f150d_brt_cosmos_362	150.1165873	2.4248924	23.98	f150d_brt_cosmos_371	150.1057684	2.4348203	24.23
f090d_brt_jsdeep_502	53.1549052	−27.7307764	22.86	f090d_brt_jsmed_132	53.14957	−27.8769106	23.19	f090d_brt_jsmed_181	53.1466098	−27.871024	23.20
f115d_brt_jsmed_262	53.0410562	−27.8377208	23.82	f150d_brt_jsmed_001	53.0413528	−28.0261991	22.93	f150d_brt_jsmed_003	53.0377722	−28.0226959	23.71
f150d_brt_jsmed_004	53.0445866	−28.0217799	23.68	f150d_brt_jsmed_009	53.0814964	−28.0060328	23.06	f150d_brt_jsmed_020	53.0568695	−27.9719865	24.66
f150d_brt_jsmed_242	53.1026077	−27.806501	24.87	f200d_brt_jsmed_004	53.066538	−28.0059346	25.84	f090d_brt_uds_021	34.3969829	−5.282103	23.75
f090d_brt_uds_130	34.3220264	−5.2457358	21.28	f090d_brt_uds_139	34.4151013	−5.2365206	22.53	f090d_brt_uds_144	34.4979806	−5.2293821	22.56
f090d_brt_uds_159	34.3708622	−5.2097999	22.55	f090d_brt_uds_216	34.2291325	−5.1644344	23.48	f115d_brt_uds_004	34.340531	−5.320432	22.29
f115d_brt_uds_009	34.5132061	−5.3191778	23.38	f115d_brt_uds_012	34.2461584	−5.3183936	24.10	f115d_brt_uds_039	34.515515	−5.3103855	23.92
f115d_brt_uds_048	34.3444628	−5.3050216	23.64	f115d_brt_uds_055	34.4625563	−5.3040264	23.80	f115d_brt_uds_059	34.5231533	−5.3030314	23.80
f115d_brt_uds_065	34.255683	−5.3017361	24.02	f115d_brt_uds_213	34.3018505	−5.2646227	23.94	f115d_brt_uds_324	34.3876199	−5.2383642	22.79
f115d_brt_uds_335	34.3040498	−5.2366875	21.16	f115d_brt_uds_346	34.2558777	−5.2338276	21.77	f115d_brt_uds_349	34.4951591	−5.2323406	23.22
f115d_brt_uds_357	34.2313445	−5.2290864	24.35	f115d_brt_uds_364	34.2692778	−5.2280467	22.29	f115d_brt_uds_416	34.2959616	−5.2127592	23.82
f115d_brt_uds_436	34.2409063	−5.2055225	23.49	f115d_brt_uds_451	34.3081378	−5.2035669	24.34	f115d_brt_uds_465	34.40423	−5.2008092	22.55
f115d_brt_uds_495	34.2351048	−5.1944463	22.96	f115d_brt_uds_500	34.3716914	−5.19226	22.81	f115d_brt_uds_537	34.4834163	−5.1786782	21.89
f115d_brt_uds_582	34.3806723	−5.1650075	22.39	f115d_brt_uds_593	34.3436309	−5.1598316	22.94	f115d_brt_uds_794	34.2278043	−5.0905055	23.58
f115d_brt_uds_797	34.3886645	−5.0868892	24.93	f115d_brt_uds_314	34.2432658	−5.239754	23.97	f115d_brt_uds_350	34.3230504	−5.2314974	24.73
f115d_brt_uds_816	34.4150182	−5.236605	25.09	f150d_brt_uds_010	34.3512775	−5.3176514	23.91	f150d_brt_uds_147	34.3383058	−5.2539202	23.95

Table A1
(Continued)

SID	R.A.	Decl.	m_{356}	SID	R.A.	Decl.	m_{356}	SID	R.A.	Decl.	m_{356}
f150d_brt_uds_195	34.2483377	−5.237603	24.18	f150d_brt_uds_196	34.4152814	−5.2363373	24.74	f150d_brt_uds_197	34.2596709	−5.2345851	25.11
f150d_brt_uds_207	34.3001351	−5.2301039	23.51	f150d_brt_uds_236	34.279762	−5.2150263	24.48	f150d_brt_uds_264	34.4928449	−5.1957711	24.60
f150d_brt_uds_282	34.325191	−5.184433	24.18	f150d_brt_uds_289	34.5235392	−5.1804038	24.75	f150d_brt_uds_291	34.4908477	−5.1794282	24.66
f150d_brt_uds_389	34.2716179	−5.1282498	25.68	f150d_brt_uds_391	34.2714136	−5.1271676	25.44	f150d_brt_uds_443	34.3813041	−5.0919038	24.12
f150d_brt_uds_447	34.4178077	−5.0894718	24.82	f150d_brt_uds_452	34.3945399	−5.0776618	22.70	f150d_brt_uds_187	34.2432052	−5.2397594	25.54
f150d_brt_uds_279	34.4877694	−5.1845142	24.52	f200d_brt_uds_087	34.4940772	−5.2783977	25.20	f200d_brt_uds_183	34.3763787	−5.2370853	25.67
f200d_brt_uds_518	34.2105	−5.0931469	25.61	…	…	…	…	…	…	…	…

Appendix B
Very Bright Dropouts in the "Undecided" Category in the Main Sample

The objects in the main sample that cannot be placed in either the "high-z" or the "low-z" categories were assigned as "undecided," which are given in Table B1 below.

Table B1
Objects in the "Undecided" Category

SID	R.A.	Decl.	m_{356}	SID	R.A.	Decl.	m_{356}
f115d_brt_ceers_430	214.751589	52.8299477	24.90	f150d_brt_ceers_113	214.8296653	52.8207925	24.11
f150d_brt_ceers_163	214.7678858	52.8163009	25.70	f090d_brt_cosmos_244	150.0775622	2.264394	25.13
f090d_brt_cosmos_351	150.0850761	2.2854155	23.15	f090d_brt_cosmos_363	150.0708811	2.2893357	23.40
f090d_brt_cosmos_395	150.0994053	2.2972383	23.20	f090d_brt_cosmos_419	150.098576	2.3012176	23.10
f090d_brt_cosmos_498	150.1762613	2.3194308	24.27	f090d_brt_cosmos_790	150.1835939	2.3903725	25.12
f090d_brt_cosmos_796	150.1557834	2.392438	24.52	f090d_brt_cosmos_919	150.1642394	2.4531855	23.51
f090d_brt_cosmos_927	150.1848911	2.4604111	25.25	f115d_brt_cosmos_010	150.0971618	2.1745523	23.54
f115d_brt_cosmos_344	150.14326	2.3560209	23.04	f150d_brt_cosmos_231	150.1819653	2.3355567	23.68
f150d_brt_cosmos_368	150.13919	2.4319799	21.61	f150d_brt_cosmos_394	150.1472663	2.4740686	24.45
f090d_brt_jsdeep_283	53.2063219	−27.7757229	24.68	f090d_brt_jsmed_040	53.0811514	−27.902613	25.09
f090d_brt_jsmed_126	53.0528574	−27.8777309	23.45	f090d_brt_jsmed_174	53.0796299	−27.870759	24.88
f090d_brt_jsmed_186	53.1015139	−27.8699644	23.45	f090d_brt_uds_076	34.4887416	−5.2656961	25.09
f090d_brt_uds_225	34.3544488	−5.1593633	24.70	f090d_brt_uds_254	34.4897227	−5.1457693	25.09
f090d_brt_uds_260	34.3822548	−5.1435204	24.43	f115d_brt_uds_640	34.3650612	−5.1488379	22.92
f115d_brt_uds_749	34.3749038	−5.1129002	20.86	f150d_brt_uds_057	34.4969958	−5.2899889	25.46
f150d_brt_uds_097	34.3248951	−5.2712995	24.66	f150d_brt_uds_361	34.2744535	−5.1437765	23.47
f200d_brt_uds_044	34.3411055	−5.2964632	25.89	f200d_brt_uds_420	34.4054154	−5.1393098	25.55

ORCID iDs

Bangzheng Sun ⓘ https://orcid.org/0000-0001-7957-6202
Haojing Yan ⓘ https://orcid.org/0000-0001-7592-7714

References

Adams, N. J., Conselice, C. J., Austin, D., et al. 2024, ApJ, 965, 169
Alcalde Pampliega, B., Pérez-González, P. G., Barro, G., et al. 2019, ApJ, 876, 135
Arnouts, S., Cristiani, S., Moscardini, L., et al. 1999, MNRAS, 310, 540
Arrabal Haro, P., Dickinson, M., Finkelstein, S. L., et al. 2023a, Natur, 622, 707
Arrabal Haro, P., Dickinson, M., Finkelstein, S. L., et al. 2023b, ApJL, 951, L22
Barrufet, L., Oesch, P. A., Weibel, A., et al. 2023, MNRAS, 522, 449
Bertin, E., & Arnouts, S. 1996, A&AS, 117, 393
Boquien, M., Burgarella, D., Roehlly, Y., et al. 2019, A&A, 622, A103
Bouwens, R. J., Stefanon, M., Brammer, G., et al. 2023, MNRAS, 523, 1036
Brammer, G. 2023, msaexp: NIRSpec Analyis Tools, v0.6.17, Zenodo, doi:10.5281/zenodo.7299500
Brammer, G. B., van Dokkum, P. G., & Coppi, P. 2008, ApJ, 686, 1503
Brown, M. J. I., Moustakas, J., Smith, J. D. T., et al. 2014, ApJS, 212, 18
Bruzual, G., & Charlot, S. 2003, MNRAS, 344, 1000
Bushouse, H., Eisenhamer, J., Dencheva, N., et al. 2024, JWST Calibration Pipeline, v1.14.0, Zenodo, doi:10.5281/zenodo.6984365
Calzetti, D. 2001, PASP, 113, 1449
Calzetti, D., Kinney, A. L., & Storchi-Bergmann, T. 1994, ApJ, 429, 582
Caputi, K. I., Michałowski, M. J., Krips, M., et al. 2014, ApJ, 788, 126
Carniani, S., Hainline, K., D'Eugenio, F., et al. 2024, Natur, 633, 318
Chabrier, G. 2003, PASP, 115, 763
Cowie, L. L., Barger, A. J., Wang, W. H., & Williams, J. P. 2009, ApJL, 697, L122
Dekel, A., Sarkar, K. C., Birnboim, Y., Mandelker, N., & Li, Z. 2023, MNRAS, 523, 3201
Eisenstein, D. J., Willott, C., Alberts, S., et al. 2023, arXiv:2306.02465
Elston, R., Rieke, G. H., & Rieke, M. J. 1988, ApJL, 331, L77
Ferrara, A., Pallottini, A., & Dayal, P. 2023, MNRAS, 522, 3986
Ferreira, L., Adams, N., Conselice, C. J., et al. 2022, ApJL, 938, L2
Ferreira, L., Conselice, C. J., Sazonova, E., et al. 2023, ApJ, 955, 94
Finkelstein, S. L., Bagley, M. B., Arrabal Haro, P., et al. 2025, ApJL, 983, L4
Fudamoto, Y., Inoue, A. K., & Sugahara, Y. 2022, ApJL, 938, L24
Gibson, J. L., Nelson, E., Williams, C. C., et al. 2024, ApJ, 974, 48
Gómez-Guijarro, C., Elbaz, D., Xiao, M., et al. 2022, A&A, 658, A43
Gómez-Guijarro, C., Magnelli, B., Elbaz, D., et al. 2023, A&A, 677, A34
Grogin, N. A., Kocevski, D. D., Faber, S. M., et al. 2011, ApJS, 197, 35
Hu, E. M., & Ridgway, S. E. 1994, AJ, 107, 1303
Ilbert, O., Arnouts, S., McCracken, H. J., et al. 2006, A&A, 457, 841
Isobe, Y., Ouchi, M., Tominaga, N., et al. 2023, ApJ, 959, 100
Jacobs, C., Glazebrook, K., Calabrò, A., et al. 2023, ApJL, 948, L13
Koekemoer, A. M., Faber, S. M., Ferguson, H. C., et al. 2011, ApJS, 197, 36
Kuhn, V., Guo, Y., Martin, A., et al. 2024, ApJL, 968, L15
Labbé, I., van Dokkum, P., Nelson, E., et al. 2023, Natur, 616, 266
Larson, R. L., Hutchison, T. A., Bagley, M., et al. 2023a, ApJ, 958, 141
Larson, R. L., Finkelstein, S. L., Kocevski, D. D., et al. 2023b, ApJL, 953, L29
Ling, C., & Yan, H. 2022, ApJ, 929, 40
Mason, C. A., Trenti, M., & Treu, T. 2023, MNRAS, 521, 497
Nelson, E. J., Suess, K. A., Bezanson, R., et al. 2023, ApJL, 948, L18
Oke, J. B., & Gunn, J. E. 1983, ApJ, 266, 713
Robertson, B. E., Tacchella, S., Johnson, B. D., et al. 2023, ApJL, 942, L42
Rodighiero, G., Bisigello, L., Iani, E., et al. 2023, MNRAS, 518, L19
Scodeggio, M., & Silva, D. R. 2000, A&A, 359, 953
Shen, X., Vogelsberger, M., Boylan-Kolchin, M., Tacchella, S., & Kannan, R. 2023, MNRAS, 525, 3254
Stalevski, M., Fritz, J., Baes, M., Nakos, T., & Popović, L. Č. 2012, MNRAS, 420, 2756
Stalevski, M., Ricci, C., Ueda, Y., et al. 2016, MNRAS, 458, 2288
Steidel, C. C., & Hamilton, D. 1992, AJ, 104, 941
Steidel, C. C., & Hamilton, D. 1993, AJ, 105, 2017
Steidel, C. C., Pettini, M., & Hamilton, D. 1995, AJ, 110, 2519
Tang, M., Stark, D. P., Chen, Z., et al. 2023, MNRAS, 526, 1657
Thompson, D., Beckwith, S. V. W., Fockenbrock, R., et al. 1999, ApJ, 523, 100
Walter, F., Decarli, R., Carilli, C., et al. 2012, Natur, 486, 233
Wang, T., Elbaz, D., Schreiber, C., et al. 2016, ApJ, 816, 84
Wang, T., Schreiber, C., Elbaz, D., et al. 2019, Natur, 572, 211
Wang, W.-H., Barger, A. J., & Cowie, L. L. 2012, ApJ, 744, 155
Williams, C. C., Oesch, P. A., Weibel, A., et al. 2025, ApJ, 979, 140
Xiao, M. Y., Elbaz, D., Gómez-Guijarro, C., et al. 2023, A&A, 672, A18
Yan, H., Ma, Z., Ling, C., Cheng, C., & Huang, J.-S. 2023a, ApJL, 942, L9

Yan, H., Sun, B., & Ling, C. 2024, ApJ, 975, 44
Yan, H., Sun, B., Ma, Z., & Ling, C. 2023b, arXiv:2311.15121
Yan, H., Dickinson, M., Eisenhardt, P. R. M., et al. 2004, ApJ, 616, 63
Yan, L., McCarthy, P. J., Weymann, R. J., et al. 2000, AJ, 120, 575

Yang, G., Papovich, C., Bagley, M. B., et al. 2023, ApJL, 956, L12
Zavala, J. A., Buat, V., Casey, C. M., et al. 2023, ApJL, 943, L9
Zhou, L., Elbaz, D., Franco, M., et al. 2020, A&A, 642, A155
Zitrin, A., Labbé, I., Belli, S., et al. 2015, ApJL, 810, L12